

QATAR UNIVERSITY

COLLEGE OF ENGINEERING

MECHANICAL AND ENERGY ABSORPTION PROPERTIES OF 3D-PRINTED

HONEYCOMB STRUCTURES WITH VORONOI TESSELLATIONS

BY

ABDELRAHMAN MOHAMED RAGAB MOHAMED AHMED

A Thesis Submitted to

the College of Engineering

in Partial Fulfillment of the Requirements for the Degree of

Masters of Science in Mechanical Engineering

January 2022

© 2022 Abdelrahman Mohamed Ragab Mohamed Ahmed. All Rights Reserved.

COMMITTEE PAGE

The members of the Committee approve the Thesis of
Abdelrahman Mohamed Ragab Mohamed defended on 23/11/2021.

John-John Cabibihan
Thesis/Dissertation Supervisor

Jamil Renno
Committee Member

Raffaello Furlan
Committee Member

John Ryan Dizon
Committee Member

Approved:

Khalid Kamal Naji, Dean, College of Engineering

ABSTRACT

AHMED, ABDLERAHMAN MOHAMED RAGAB MOHAMED, Masters : January : [2022], Masters of Science in Mechanical Engineering

Title: Mechanical and Energy Absorption Properties of 3D-Printed Honeycomb Structures with Voronoi Tessellations

Supervisor of Thesis: John-John, Cabibihan.

3D printing is the new frontier in building construction. It is especially useful for building small houses within a short period of time. Complete construction including the interior partitions and exterior facade can be achieved with 3D printing. In this thesis, a parametric Voronoi model is proposed for quickly generating and fabricating 3D printed partitions for interior design. Parametric design allows rapid customization and enables manufacturing of unique structures with 3D printing. This technique allows for the fabrication of complex designs that would be difficult to fabricate with traditional manufacturing methods. Furthermore, the fabricated Voronoi structures are aesthetically pleasing and exhibits artistic expressions while maintaining structural integrity. Modular design allows different type of structural designs as needed with easy assembly using magnetic coupling. This study introduces a parametric design of a hexagonal block with an enclosed surface of relaxed Voronoi cells. A number of those blocks have been manufactured through a 3D printing process to be puzzle-like assemblage, producing a large-scale cohesive artistic wall. This study provides comprehensive and comparative testing to ensure the validity of the mechanical properties of the design and investigating the energy absorption characteristics for the proposed 3D printed hexagonal block. The best Voronoi structures exhibit superior mechanical and energy absorption properties compared to their non-Voronoi counterparts with energy absorption values ranging from 350 J to 435 J and crash force

efficiency being 1.42 to 1.65.

DEDICATION

I dedicate this thesis to my father, whom I wished to see it, my mother and my wife..

ACKNOWLEDGMENTS

This last year was extremely difficult for me, as all of my family got infected with Corona exactly after submitting my first progress report, and unfortunately, my father couldn't make it. I lost him last year, but his soul remained with me the whole time. I am very grateful for my father, Dr Mohamed Ragab, for all his support and love for me, for everything he has given me across my whole life, for everything. Without him, I would not have finished my master's degree, nor would I have achieved what I have achieved. I would also like to extend my thanks to my mother, Mrs Mona Farouk, for being by my side and giving me all the love, support, and pride in me and fighting for me and getting me to the present moment. I would also like to extend a special thanks to my best friend, companion and partner, my wife, the artist Esraa Abdelfatah, for always standing by my side, helping me through difficult times, offering unconditional love and her constant pride in me and my work. She is my personal source of my inspiration, encouragement, and ambition. Also, I am extremely grateful to my thesis supervisor Dr John-John Cabibihan for the extensive support, guidance, and mentorship that he has provided me during my master's program. I learnt from him many valuable skills during my work with him in my thesis and other projects. I thank Prof. Sadig for his help and insights during the experimental part. Also, I am grateful to my friend Eng. Mohammed Houkan for providing the support, encouragement, constructive feedback, and his help in the 3D printing process. I thank my friend Eng. Islam Ibrahim for his support and encouragement. I thank my friend Eng. Mohammed Mudathir for his useful insights and advice. I would like to acknowledge the Department of Mechanical and Industrial Engineering, my great instructors, and my colleagues for their support and kindness. I am sincerely grateful to you all. Thank you.

This thesis was supported by the NPRP grant # NPRP 11S – 1229 – 170145 from the Qatar National Research Fund (a member of Qatar Foundation). The statements made herein are solely the responsibility of the authors.

TABLE OF CONTENTS

DEDICATION	v
ACKNOWLEDGMENTS	vi
LIST OF TABLES	x
LIST OF FIGURES	xi
CHAPTER 1: INTRODUCTION	1
Aim and Objectives	3
Organization of Chapters	4
Chapter 2: Background and related work	5
3D Printing	5
Tensile Test for 3D Printed Material.....	7
Load-Carrying and Energy Absorption Capacities Investigations for 3D Printed Structures.....	12
Chapter 3: Methodology	18
Proposed Design.....	18
Parametric Modeling	18
3D Model of the Hexagonal Honeycomb.....	24
Magnetic Convention	25
3D Printing	28
Tensile Test	30
Preparation of Test's Specimens	30
Test setup.....	32

Test Parameters.....	33
Energy absorption testing experimental setup	34
Preparation of Test’s Specimens	34
Test Setup	40
Energy Absorption Parameters	41
Chapter 4: Results and Discussion.....	43
3D Printed Prototype.....	43
Results of Experimental Tests.....	45
Tensile Test Results.....	45
Energy Absorption Results.....	50
Stress Analysis.....	58
Energy Absorption Performance Discussion.....	60
Chapter 5: Conclusion, Contribution of Knowledge, And Future Work.....	65
References.....	67
Appendix A: The Crushing behaviour under compression.....	74
Appendix B: Average Force and displacement curves	79
Appendix C: Some Printed Samples that Obtained During the Trial-and-Error Phase	80

LIST OF TABLES

Table 1: Summary of some previous studies that conducted a tensile test on 3D printed material.	11
Table 2: Setting of the 3D printing process	29
Table 3: Typical ranges of mechanical properties for PLA material [53].	29
Table 4: Weights of the tensile specimens.....	32
Table 5: Grouping and description of the experimental samples while showing the 3D models.....	37
Table 6: Weights of the compression specimens.....	39
Table 7: Tensile properties obtained from the conducted tensile tests.	49
Table 8: Experimental energy absorption results for each sample and the mean SEA for each group.....	56
Table 9: Values of initial peak force for each sample, and the mean for each group..	57
Table 10: The average of applied forces on every sample and the calculated mean of CFE.	57
Table 11: Crushing behaviour of all honeycomb samples with different configurations under quasi-static axial compression.	74

LIST OF FIGURES

Figure 1: A fully 3D printed green wall [2].	2
Figure 2: Full Grasshopper algorithm to create the proposed Voronoi tessellations.	19
Figure 3: Generating random points on spiral lines – “Points on spiral lines” cluster.	20
Figure 4: Generated random points within the hexagonal frame.	20
Figure 5: The initially generated tessellations.	21
Figure 6: Lloyd’s algorithm to get the relaxed Voronoi tessellation – “Lloyd’s algorithm” cluster.	21
Figure 7: The relaxed Voronoi tessellation generated using Lloyd’s algorithm.	22
Figure 8: Pushing the Voronoi cells to edges and optimizing the final weight – “Modified distribution” cluster.	22
Figure 9: The Voronoi cells distribution in different number iterations shows almost the loop function's convergence.	23
Figure 10: The Voronoi tessellation's final design is used later to fill the hexagonal honeycomb.	24
Figure 11: 3D model of the presented hexagonal honeycomb with the dimensions [mm].	24
Figure 12: 3D model of the presented hexagonal honeycomb after including the magnet slots.	26
Figure 13: The arrangement of the front, rear and internal coupling, respectively, as the letter (N) and blue colour refer to the north pole of the magnet while the letter (S) and red colour refer to the south pole.	27
Figure 14: Snapshot of the interface of Cura software.	28
Figure 15: Geometrical data (in mm) of the dog bone specimen for the tensile test according to ASTM D638 – 14 (Type I).	30

Figure 16: 3D printing the test specimens.	31
Figure 17: 3D printed tensile test's specimens.	31
Figure 18: Specimen positioned and ready to be tested.....	33
Figure 19: Dividing the proposed honeycomb to obtain the compression specimens. Where (w) refers to having slots, and (w/o) refers to not having ones.	34
Figure 20: The two types of design for the compression specimens.	35
Figure 21: Geometrical data (in mm) of all compression test samples.....	36
Figure 22: A 3D printed sample from each group.	39
Figure 23: The setup of the compression testing.	40
Figure 24: 3D printed prototype of the interior partition.	44
Figure 25: 3D printed prototype of the interior partition.	44
Figure 26: Test specimens after the tensile testing.	45
Figure 27: Stress-strain (σ - ϵ) tensile test curves for the three samples.	47
Figure 28: The regression line of the initial linear part of the stress–strain curve, is represented as dotted line, which is used for the calculation of E.	48
Figure 29: Force and displacement curves for Group A, honeycombs with Control configuration, slots are not included.	51
Figure 30: Force and displacement curves for Group B, honeycombs with Beam configuration, slots are not included.	51
Figure 31: Force and displacement curves for Group C, honeycombs with Column configuration, slots are not included.	51
Figure 32: Force and displacement curves for Group D, honeycombs with Cross configuration, slots are not included.	52
Figure 33: Force and displacement curves for Group E, honeycombs with Voronoi tessellation configuration, slots are not included.	52

Figure 34: Force and displacement curves for Group F, honeycombs with Control configuration, slots are included.	52
Figure 35: Force and displacement curves for Group G, honeycombs with Beam configuration, slots are included.	53
Figure 36: Force and displacement curves for Group H, honeycombs with Column configuration, slots are included.	53
Figure 37: Force and displacement curves for Group I, honeycombs with Cross configuration, slots are included.	53
Figure 38: Force and displacement curves for Group J, honeycombs with Voronoi tessellations, slots are included.	54
Figure 39: A snapshot of the crashing process of one sample from Group D.	55
Figure 40: Section view of the 3D model used for simulation.	58
Figure 41: Contour plot that shows the stress concentrations in the front surface of Group J.	59
Figure 42: Contour plot that shows the stress concentrations in the front surface of Group E.	59
Figure 43: Bar charts summarizing the performance levels in terms of energy absorption.	60
Figure 44: Bar charts summarizing the performance levels in terms of SEA.	61
Figure 45: Bar charts summarizing the performance levels in terms of IPF.	63
Figure 46: Bar charts summarizing the performance levels in terms of CFE.	63
Figure 47: Average Force and displacement curves for all Groups, while slots are not included.	79
Figure 48: Average Force and displacement curves for all Groups, while slots are included.	79

Figure 49: Printed samples with different infill.....80

Figure 50: Printed samples with different layer heights80

CHAPTER 1: INTRODUCTION

Additive manufacturing or 3D printing technology allows manufacturing of structures using digital models without using costly manufacturing machines, is used worldwide and plays an essential role in fabrication and manufacturing in different fields [1]. Furthermore, 3D printing technology becomes progressively more used for mass customization, the production of various complex designs in the agricultural, healthcare, automotive, and aerospace industries. Moreover, the 3D printing additive manufacturing process deposits only materials where and as needed, making it more cost-efficient than other manufacturing methods.

Using 3D printing technology to scale up to the level of complete and large structures has to be based on several scheduled innovations in the field of:

1. lean parametric design to production processes, saving money, time, and resources.
2. the smart integration of cultural-aesthetic, structural and climatic performance in the 3D printed structures components.
3. the assembly of prefabricated integrated 3D printed elements into large-scale building complexes by applying the state-of-the-art principles of mass customization.

Additionally, parametric design in combination with 3D printing allows each building component to have a unique structure and unique customized finishing pattern, therewith bringing back the visual and tectonic qualities of expert handicrafts of earlier days. Moreover, there should be more usage of 3D printing technology combined with parametric design in building architectural structures such as facades, interior walls, and interior partitions. Because that 3D printing technology is cheaper than other traditional costly manufacturing machines [1]. For example, a fully 3D printed green

wall that has an embedded irrigation and drainage system is shown in Figure 1.



Figure 1: A fully 3D printed green wall [2].

Although there are a lot of advantages to 3D printing, the optimization between the mechanical properties of printed structures and cost and time could be challenging. Hence, the mechanical properties of the 3D printed structures should be investigated and analyzed in order to indicate their reliability for different manufacturing purposes. There are a considerable number of 3D printing parameters that have direct and indirect effects on the mechanical properties of the 3D printed material. For instance, increasing the infill density would increase the strength, but it would increase the material consumption and cost. Thus, optimization should be considered based on the application and usage of the 3D printed parts. In addition, material testing such as tensile tests would have different results for any minimal change in the settings of the 3D printing parameters.

Additionally, some properties should be considered while designing 3D printed structures, such as the energy absorption capacity and load-carrying capability. Energy absorption characteristics are essential to be investigated for many applications in

various fields such as construction, aerospace, automotive and many other technology fields. For the architecture static buildings or structures, it is desirable and required to have high energy absorption structures made from ultra-light material. Those structures are supposed to carry a relatively high load in a specified space. It is mainly affected by the geometry of the structure, so investigating the amount of absorbed energy for a particular structure would indicate the stability and strength of the structure. Moreover, it would help if some particular structure would require more support or core filling during the designing process.

Overall, the research question of this thesis will be, if there is a hexagonal structure, what would be the best filling that will produce the best energy absorption performance? Laban et al. (2021) [3] conducted recent research that investigated the energy absorption performance of four different hexagonal configurations (coreless, column, beam and cross), and it was reported that the cross design has the highest energy absorption value. However, here in this research, an investigation of a hexagonal honeycomb filled with Voronoi tessellation will be presented and compared with Laban's designs.

Aim and Objectives

The aim of this thesis is to investigate how to produce Voronoi structures with good energy absorption and mechanical properties using 3D printing while obtaining a lightweight structure. To achieve this goal, an investigation has been conducted for the energy absorption performance and load-carrying capability of a 3D printed hexagonal honeycomb filled with Voronoi tessellations through a comparative study with other hexagonal honeycomb but with different fillings. Additionally, another investigation has occurred on the tensile properties of the printed PLA while using the same printing settings used for prototypes. To achieve the lightest weight possible, testing was done

with a 10% infill which is lacking in the literature.

The objectives of the research are as follows:

1. Design the presented hexagonal honeycomb, using parametric design methodologies.
2. 3D printing the prototype, tensile specimens, and compression specimens with 10% infill.
3. Conduct a tensile test to get the mechanical properties of the printed PLA.
4. Conduct an experiment of applying quasi-static axial compression to investigate the energy absorption performance for different honeycombs.

Organization of Chapters

This thesis is organized into several chapters. In this introduction chapter, an overview of the thesis is presented, including the motivation behind this research as well as a short discussion of key points, which will be discussed in later chapters. Chapter 2 covers a comprehensive literature review on tensile tests for 3D printed material and how printing parameters could affect its properties. Additionally, it covers a number of different studies that investigated energy absorption characters of 3D printed structures. Chapter 3 describes the methodology, including different sections to discuss the proposed design, tensile test setup, and compression experiment setup. Chapter 4 include results that highlight the findings of each method while discussing the results and the decisions that were made throughout this research. Chapter 5 concludes the thesis and suggests possible future works.

CHAPTER 2: BACKGROUND AND RELATED WORK

3D Printing

3D printing has come a long way since its inception in the 1980s [4][5]. It is a unique and novel additive manufacturing technology that allows creating of structures and objects using digital models without the need for traditional costly manufacturing machines [1]. Moreover, 3D printing technology has grown exponentially in recent years and continues to grow due to its versatility and low cost for rapid prototyping and manufacturing applications [1][6][7]. Moreover, 3D printing has absolute advantages in manufacturing complex shapes and multi-material parts, compared with any other manufacturing technology [7][8]. Recently, there has been a considerable increase in the usage of 3D printers that come with a variety of printing materials, configurations, and types [6]. Additionally, they are often used in various fields such as biomedicine [9], digital art, architectural design, food industry [10], aerospace, automotive and many others [11][12][13]. Additionally, 3D printing technology has shown a lot of development on the stiffened structural designs that have been deployed in the construction and architecture fields [14][15] [13].

There are different 3D printing types, such as Deposition Modelling (FDM), Fused Selective Laser Sintering (SLS), and Selective Laser Melting (SLM) which are solid based technologies where Stereolithography (SLA) is a liquid based method that cures a polymer [16][17]. Additionally, there are other methods of additive manufacturing based on ISO/ASTM 52900 standard such as binder jetting and powder bed fusion [18]. In this research, the discussion will be mainly on the FDM method. It is currently the most applied method among the other techniques, especially for prototyping purposes [16]; it has become one of the most famous 3D printing techniques worldwide [19]. Moreover, FDM technology depends on the layer-by-layer

building or addition process, using an extruded filament. For instance, the raw material has to go through an extrusion process into the nozzle. Then, it would be transformed from the original filament state to the semi-liquid state, which is deposited into the existing layer cooled to be solidified and integrated with other layers. After finishing every layer, the extruder moves upwards, or the platform itself goes down to one layer's thickness (one layer height). Due to the wide application of this method in rapid prototyping [20], various polymers are used for FDM, such as (polylactic acid (PLA), acrylonitrile butadiene styrene (ABS), polypropylene (PP), polyamide (PA)), polymer ceramic and matrix composites, nanocomposites, and fibre-reinforced composites, according to [21].

FDM parameters can be divided into three different classifications, as reported in a recent review [13]:

1. Slicing parameters, which includes: layer height, infill characteristics (speed, density, pattern), raster angle, nozzle diameter, air gap and other different parameters.
2. Building orientation, as the parts could be printed in various directions and along different axes.
3. Temperature: this includes surrounding, extruding and platform temperatures.

All of those parameters affect the bonding of the filament, which impacts the material and mechanical properties of the final printed part. The relation between some of those factors and mechanical properties of the printed material has been discussed in more detail in the following section Overall, FDM is an efficient and relatively cheap manufacturing technology.

Tensile Test for 3D Printed Material

Many studies [12], [22], [23] investigated the energy absorption characteristics tested the material properties for the printed structures through conducting a tensile test. Material properties such as tensile strength, yield strength, and modulus of elasticity could change through the 3D printing process by changing infill (density or pattern), layer heights, temperatures, and other parameters [24]. Furthermore, research investigating those relations between the mechanical properties for printed structures and 3D printing parameters and its techniques is limited, according to [24]. However, there are some researches have conducted to investigate the effects of some of those parameters on the mechanical properties for specific printed material, such as, the effect of varying infill density [24][25][26][27][28][29][16][7][30], infill pattern[24][27][29][7], raster angle/building orientation [19][31][32][30][33], layer height [28][19][30][33], infill speed [28][7][34].

Generally, infill density could have a significant effect on the mechanical performance of the printed structures[16]; decreasing the infill density would reduce the tensile strength [29][30]. A wide range of percentages of the infill density was investigated by various researchers with different results. For example, some suggested that having 80% infill density for PLA material would be the optimum percentage as it would have better stiffness and strength [26][28]. However, it would be more brittle [28]. It has been noted that as the percentage of the infill density increased from 75% to 100%, tensile strength and elastic modulus would sharply increase by almost double the amount, according to [27].

Moreover, Tanveer et al. [25] showed a wide range of tensile strength values varying from 46.3 MPa to 29.9 MPa, and they suggested that having variable infill density would provide higher values of tensile strength than single infill density [25].

Additionally, it would save the consumed material, as having variable infill density would result in lighter weight [25]. It is important to notice that all of the previously mentioned studies investigated only infill percentages from 20% to 100% while neglecting the lower infill densities. Such infill densities could be required in some applications that are not required to withstand high forces, such as some architectural interiors or designs.

Infill pattern is an essential factor in the 3D printing process. It has a significant effect on the tensile strength and elastic modulus [24][35]. According to [24] and [27], the concentric pattern was recommended as it has higher mechanical properties than other different patterns, while the grid or lattice pattern is the second in both studies. However, another research found out that tensile strength for grid pattern would be higher than the concentric one [35]. Moreover, there is a considerable number of different infill patterns; one could choose the optimum pattern, depending on the application, weight constraints and required stiffness. In addition, some patterns would have higher tensile properties with some specific material and lower values with different materials [35].

Another significant parameter on the mechanical properties is the layer height [33], as the ultimate tensile strength of printed PLA would decrease when the layer height increases or the layer becomes thicker [19] [33][36]. Having a thinner PLA layer would result in higher tensile strength. However, it would increase the printing time. In addition to that, using different materials could lead to totally different results, as using carbon fibre–PLA composite material would increase the tensile strength if the layer height got increased, as reported in [30]. Moreover, it was reported [28] that reducing the layer height for PLA would have a slight increase in the modulus of elasticity, but it would have a huge effect on the ductility properties.

Abeykoon et al. [7] have investigated a range of 70 mm/s to 110 mm/s infill speeds using PLA material, and they reported that at a speed of 90 mm/s, the tensile modulus reached the highest value[7]. Another research [34] investigated two infill speeds, 40 mm/s and 50 mm/s, and the result showed that the higher speed would have the highest tensile strength. Another investigation [28] went to even a lower range of infill speeds (20 mm/s and 40 mm/s).

A study that was conducted to investigate different FDM effects, such as raster angle, on the tensile properties of polycarbonate material showed that the tensile properties have changed by a percentage of 70% to 75% from the extruded material [37]. Raster angle is the angle between the nozzle path and the x-axis of the 3D printing platform [38][33]. Moreover, it was reported [33] that using a raster angle of 0 degrees would have the highest tensile strength. T. Yao et al. [19] agreed with [38], as this orientation showed higher mechanical properties as well. However, their definition of the angle was slightly different than [38]. Generally, for PLA, decreasing the raster angle would increase the ultimate tensile strength, as reported in [19] and [33]. Additionally, a similar investigation could be conducted on different materials other than PLA, and the result would be different [32]. Furthermore, changing the building direction (axis) would also lead to further changes in the ultimate tensile strength as the modulus of elasticity as well, as investigated in [30][32].

Other 3D printing and FDM factors affect mechanical properties such as extrusion temperature, material, nozzle diameter, raster width and various other parameters [39][40]. Recent studies have investigated those parameters and their relation with mechanical strength, such as [39][41]. Moreover, some researchers studied the interactions between some of those parameters and their influence on each other and their influence on the final manufactured part [7][40][33].

The cost and time of the FDM process are essential to consider while optimizing the other factors. For instance, increasing infill density would enhance the tensile properties, but it would require more material, which means more cost and time [7]. Moreover, using the standard infill density of 10% to 25% would manufacture the part in the quarter of the time required for the totally solid structure [29]. Decreasing layer height would improve the tensile strength for PLA and the final quality. However, it would increase the number of layers, cost, and time as well. Configuring the parameters of FDM would require optimization and consideration for the time and cost constraints. In some applications, the printing time is more critical than the strength, or the cost or maybe another specific parameter, so it is depending on the application and the purpose of the manufacturing.

To sum up this section, it is recommended that the material properties for 3D printed parts should be tested for any related 3D printed material research or investigation. As there are a lot of parameters are affecting the mechanical properties of the printed material, which differ – as discussed earlier – from the original raw material. In addition to that, there is a limited number of studies that reported actual experimental results [7]. Meanwhile, it is challenging to predict the accuracy of FDM technology and techniques because these processes are associated with many highly interdependent variables. Hence, unless another research provides the experimental tensile properties for the exact same printing configuration and material, a tensile test should be conducted for the printed parts.

Overall, Table 1 summarizes some previous studies on tensile testing of 3D printing materials (mainly PLA) and shows the results of their ultimate tensile strength and modulus of elasticity values.

Table 1: Summary of some previous studies that conducted a tensile test on 3D printed material.

Ref.	Author (Year)	Material	Standard Code (Type)	UTS [MPa]	E [MPa]
[16]	Elmrabet and Siegkas (2020)	PLA, TPU95A	ISO-527 (1A & 1B), ISO-37:2017 (2)	15.50 – 72.20	2020 – 4000
[23]	Santos et al. (2021)	PLA	ASTM D638 (Type IV)	50.23	2750
[27]	Seol et al. (2018)	PLA	ASTM D638 (Type I)	17.80 – 50.10	367.7 – 969.2
[28]	Rarani et al. (2020)	PLA	ASTM D638 (Type I)	13.88 – 44.07	1197 – 3274
[24]	Rismalia et al. (2019)	PLA	ASTM D638 (Type I)	28.10 – 33.30	2760 – 3280
[30]	Kamaal et al. (2021)	Carbon fibre-PLA composite	ASTM D638	25.04 – 46.26	--
[31]	Wahid et al. (2020)	PLA	ASTM D638 (Type IV)	26.40	2300
[33]	Rajpurohit and Dave (2019)	PLA	ASTM D638 (Type I)	21.94 – 47.30	--
[34]	Ansari and Kamil (2021)	PLA	ASTM D638 (Type IV)	40.03 – 59.84	--
[35]	Yeoh et al. (2020)	PLA and cPLA	ASTM D638	15.62 – 23.41	--
[36]	Chacón et al. (2017)	PLA	ASTM D638	20.20 – 89.10	3266 – 4409

Load-Carrying and Energy Absorption Capacities Investigations for 3D Printed Structures

The energy absorption, load-carrying capacity and crashing efficiency are very important characteristics to the designing process of many applications in various fields such as construction, aerospace, automotive and many other technology fields[42].

Having high energy absorption structure made from ultra-light material is desirable and required, especially for the architecture static buildings or structures that are supposed to carry a relatively high load in outdoor space. A study in 2014 [43] investigated the characteristics of energy absorption for honeycomb structures. Moreover, five different geometries of honeycombs were presented: square, triangular, circular, hexagonal, and kagome. Using an FEA simulation, the deformation mechanism and absorbed energy were investigated. Moreover, the results showed that kagome honeycomb has the highest value of specific energy absorption. Moreover, the hexagonal and triangle structures have the second-highest value for energy absorption capacities as well as load carrying, with a minimal difference between both structures. However, the hexagonal honeycomb has higher stability in the stress plateau. They [43] reported that the hexagonal honeycomb would be considered one of the ideal structures for an energy absorption application, while the square geometry was not recommended for such application.

A more recent study [44] had a deeper investigation about the energy absorption of honeycomb structures. The study proposed nine different honeycomb geometries to study their mechanical behaviour regarding their absorbed energy capacities through non-linear numerical simulations. Additionally, the plateau stresses were investigated as well for the nine geometries in order to check the stability and compressibility of the plateau stress. It was reported in [44] that hexagonal honeycomb has the highest plateau stress with an ideality percentage of 80%; also, it has the highest absorbed energy

among the other nine honeycombs. Generally, they [44] reported that hexagonal honeycomb would have the ideal honeycomb structure for energy absorption application, as well as the most stable and almost constant plateau stress with great compressibility.

Many researchers have investigated those characteristics by conducting compression tests for 3D printed structures to get their beneficial mechanical properties [12] [3] [45] [46] [47] [48] [49] [23] [50] [22], such as Initial Peak Force (IPF), Specific Energy Absorption (SEA), and Crash Force Efficiency (CFE). Moreover, the investigated printed parts have different geometries and shapes that have been emerged from nature or numerical topology optimization or parametric design to be used in structural applications.

Habib et al. [45] conducted a Uniaxial quasi-static compression test on 3D printed hexagonal honeycomb structures, with different wall thicknesses in different orientations, along with numerical simulations. The numerical, analytical, and experimental results were very close, indicating that the hexagonal honeycomb's mechanical behaviour was predictable. Results indicated that there were two different orientations for the hexagons, one has the flat surface as top, and the other has the corner one. The flat-top had higher stability and higher values of energy absorption and stress plateau [44], [45].

A honeycomb structure has been printed using the FDM method, and then its mechanical behaviour has been investigated according to Antony et al. [46]. Moreover, compression and bending tests have been conducted on the structure within different orientations [46]. Additionally, a tensile test with different infill angles has been conducted. However, only the hexagonal shape was addressed, and no other geometries have been investigated [46].

Podroužek et al. [47] did a compression test for 14 cylinders with different infill patterns, including gyroids and hexagonal shapes. They compared the 2D hexagonal pattern and the 3D gyroid. They considered the 3D gyroid to be better in the mechanical characteristics, especially if the final shape is complex with various orientations [47].

Yang et al. [48] investigated the mechanical behaviour of 3 different auxetic structures under the impact and compression force. Furthermore, their three auxetic structures were in the shape of the hexagonal honeycomb, arrowheads, and re-entrant hexagons. Static and dynamic analysis was conducted for the FEA models, then it was validated by experimental 3D printed structures printed in three different materials, such as PLA [48].

According to [49], four pore shapes such as hexagonal, cylindrical, triangular and square were exposed to an investigation of their energy absorption behaviour through a uniaxial compression test. Moreover, the samples were printed by FDM using ABS material. The results showed that the hexagon (honeycomb) shape has the highest compressive yield strength and exceptional energy absorption.

Another study was conducted of Nylon and Al/Nylon 3D printed tubes with different inner structures, which are single and quadruple cells tubes [12]. The characteristics of energy absorption of the tubes were investigated while conducting the tensile test for the material as well. Moreover, their result suggested the hybrid material with quadruple-cell would be better for energy absorption, as they have higher energy absorption efficiency [12].

Through quasi-static indentation and low-velocity dynamic tests, Santos et al. [21] tested 3D PLA, and PETg printed layered structures with different core tessellations for energy absorption characteristics. There were two types of tessellations, the honeycomb hexagonal and re-entrant hexagonal geometries. The

results indicated that the PETg material has a higher impact protection ability than the PLA material. Furthermore, the re-entrant hexagonal structures showed generally higher dissipated energy than the honeycomb ones.

Another energy absorption investigation has been conducted for 3D printed PEEK and CF/PEEK material cellular composites [50]. Moreover, quasi-static compressive and low-velocity impact tests were conducted on hexagonal, chiral and re-entrant unit cell structures. It was reported [14] that CF/PEEK has higher specific energy absorption (SEA) by five times. Furthermore, the SEA has had the highest value for the hexagonal structure with PEEK material for both the In-plane and out-of-plane performances, also with CF/PEEK material for the out-of-plane performance. However, it had the lowest value with PEEK material in the in-plane performance.

The honeycomb structure was tested according to [22] with another two auxetic cellular structures. Moreover, PLA, PLA-Nylon and PLA-TPU materials were used to 3D print three different specimens for each design or structure. Additionally, a quasi-static compression test has been conducted on all the samples with a compression rate of 10 mm/min and a crashing portion of 85%. After repeating the test three times for each sample, the force and displacement data were extracted. The results showed that the test for honeycomb hexagonal structures was repeatable for PLA and PLA-TPU material, but not for the PLA and Nylon as the material did not stick with each other and showed a large variation. Furthermore, this study [22] was coupled with FEA validation. It was reported that the hexagonal structures printed with PLA material has the highest amount of absorbed energy. Generally, the PLA single material had the highest absorbed energy for a structure with single loading cycle [22].

Recent research [3] investigated the load carrying and energy absorption capacities for additively manufactured four different geometries of hexagonal

honeycomb. Moreover, two methods of additive manufacturing have been used, FDM and DMLS. An in-plane compression test has been used to get the carrying load and energy absorption characteristics for the four different geometries that are manufactured twice with polymer and metal. The results showed a comparison between the results coming out from the parts that were manufactured through FDM and others that were manufactured through DMLS. This comparison showed that adding cross configuration inside the hexagonal honeycomb would have a huge increase in SEA and IPF values comparing with the non-infilled (coreless) hexagon geometry, as the cross geometry has the highest IPF and SEA for both FDM and DMLS samples. The research [3] reported the similarity for the collapsing behaviour of the different hexagons between both sets of FDM and DMLS.

Overall, there are many geometrical optimization studies that investigated the energy absorption of different geometries [10] [19] [42] [43] [44] [23] [24] [25] [26] [27] [28] [29] [30], and some of them obtained actual experimental results [10] [19] [23] [24] [25] [26] [27] [28] [29] [30]. The previously discussed experimental studies conducted through compression test conducted on cellular structures such as honeycomb structures [19] [23][24][26] [28] [30] and others different structures [10] [25] [27]. Moreover, there are two directions for compression test has been covered, in plane [43] [43] [22] [23] [24] [26] [28] [30], which is the main focus in this research, and out plane [24] [27]. Furthermore, some of those discussed comparative studies recommended the hexagonal honeycomb structure, as it has high energy absorption capabilities, high stability, and great compressibility [22] [23]. Additionally, the recent research of [19] showed that increasing having filled hexagonal honeycomb would decrease the energy absorption as well.

To conclude, polymer honeycombs could be manufactured by FDM technology

– or 3D printing in general) – in the desired size or dimensions while having high energy absorption characteristics to be used in a specific application or study. For example, 3D printing allows us to have various geometrical architecture designs of honeycomb structures for some static structures or applications such as façade or interior partitions.

CHAPTER 3: METHODOLOGY

In this chapter, the 3D model and design of the presented honeycomb structure while mentioning the role of parametric modelling during the designing process. Secondly, the 3D printing process and parameters will be mentioned and discussed. Thirdly, the tensile test standards and the setup for 3D printed PLA material, with the same 3D printing parameters. Lastly, the experimental setup of the quasi-static axial compression testing.

Proposed Design

The proposed design is part of an interior partition that was designed and built from similar hexagonal honeycomb cells filled with Voronoi tessellations that are arranged in a repeated pattern. Each cell or block has attached to the other by using magnetic coupling that will be explained later. As discussed, the analysis in this study would be focused on the repeated hexagonal honeycomb cell. So, the modelling of this cell will be discussed in this section.

Parametric Modeling

Parametric modelling involves the development of mathematical relationships between different parameters in the geometry design, along with programming using different scripts to provide an efficient 3D model, then export it to STL to proceed with the 3D printing process. Moreover, parametric modelling has been used to create the Voronoi tessellation pattern, which is later used to fill the hexagonal honeycomb.

Rhino or Rhinoceros 3D software has been used in the designing process. Moreover, it is a 3D modelling software used to design complex products and has been developed by Robert McNeel & Associates. Additionally, it supports parametric modelling through polygonal meshes, uniform splines or Non-Uniform Rational Basis Splines

(NURBS), and that allows the software to create various designs and geometries with high mathematical precision and accurate representation [51].

Grasshopper is a plugin for Rhino software that offers a powerful set of tools to create and model complex designs; also, It was developed by David Rutten and Robert McNeel [52]. For instance, it enables visual block-based programming for parametric modelling. Moreover, it provides an algorithmic modelling method that would allow the creation of different novel structures and patterns using generative algorithms with parametric relations.

The parametric modelling for the Voronoi tessellations went through three different phases. Figure 2 is a clustered Grasshopper diagram to show the overall view of the parametric modelling. Firstly, creating an enclosed hexagon periphery and generating random points on generated spiral lines. Secondly, removing the points that generated outside the hexagon, and creating a rectangular boundary that is required to generate the Voronoi cells. Finally, initiating a loop function to:

- a) generate the Voronoi cells,
- b) use the Lloyd's algorithm to have relaxed Voronoi tessellations,
- c) modify the distribution of the cells to optimize the weight of the final design.

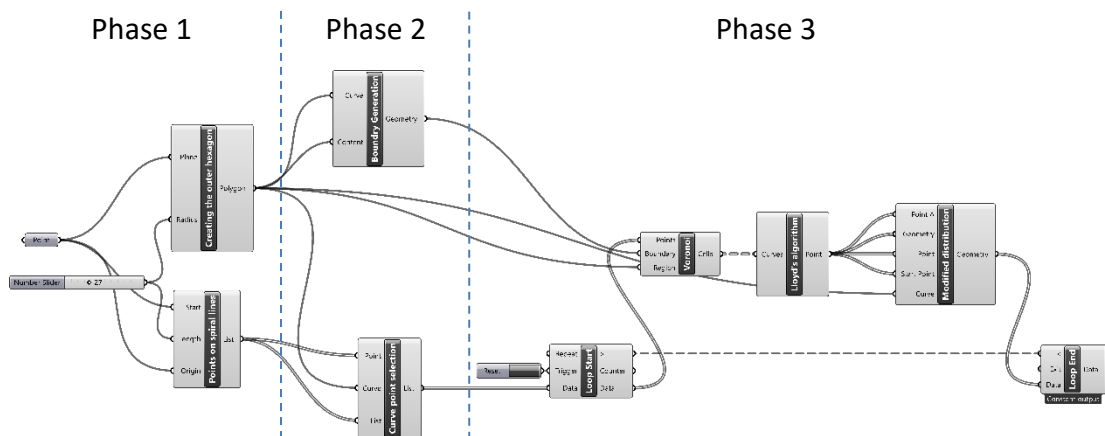


Figure 2: Full Grasshopper algorithm to create the proposed Voronoi tessellations.

Let us get a closer look at some of the main points in the mentioned overall algorithm.

After creating the hexagonal frame, - as shown in Figure 2- the cluster “Points on spiral lines” was applied, consisting of the steps mentioned in detail in Figure 3.

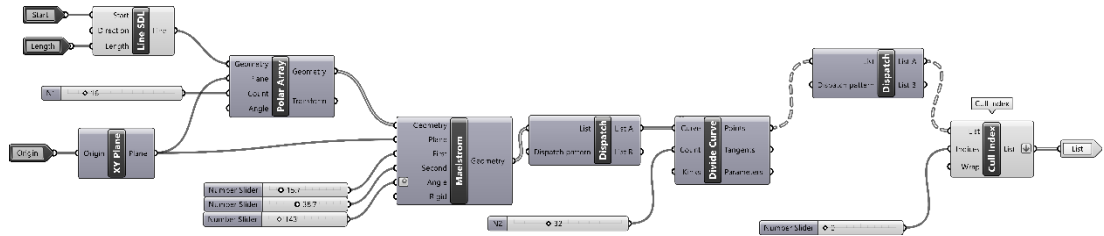


Figure 3: Generating random points on spiral lines – “Points on spiral lines” cluster.

Those points were randomly generated from the created spiral curves then all the points outside the hexagon were eliminated, resulting in the step shown in Figure 4.

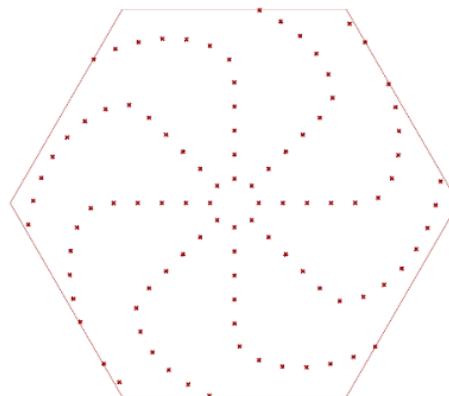


Figure 4: Generated random points within the hexagonal frame.

Then, using the Voronoi function, those points were transferred to different Voronoi cells, and a frame was created for each cell to make each one an independent periphery, as shown in Figure 5.

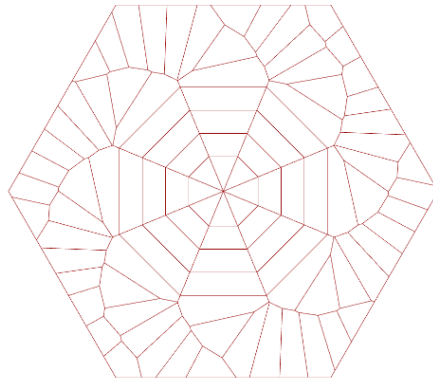


Figure 5: The initially generated tessellations.

Inside the loop function, after calling the Voronoi function, the Lloyd's algorithm was applied to have a new relaxed Voronoi tessellations using the obtained centroid of each cell.

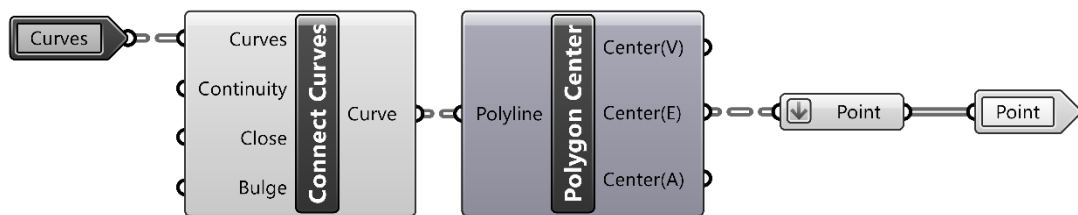


Figure 6: Lloyd's algorithm to get the relaxed Voronoi tessellation – “Lloyd's algorithm” cluster.

After applying 30 iterations in the loop function, the relaxed tessellation shown in Figure 7 was obtained.

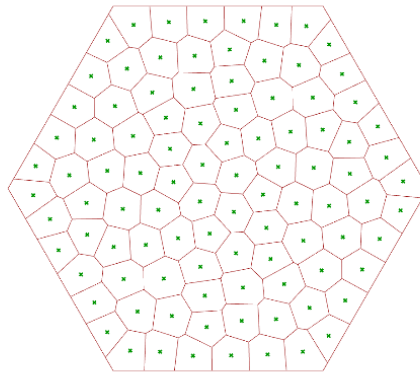


Figure 7: The relaxed Voronoi tessellation generated using Lloyd’s algorithm.

In order to optimize the weight of the final design and allow it to have more strength, the distribution of the Voronoi tessellations was modified using the operation mentioned in Figure 8. This would push the Voronoi cells to edges and increase the density of the cells nears from edges while reducing it in the center of the hexagon, which would optimize the final weight.

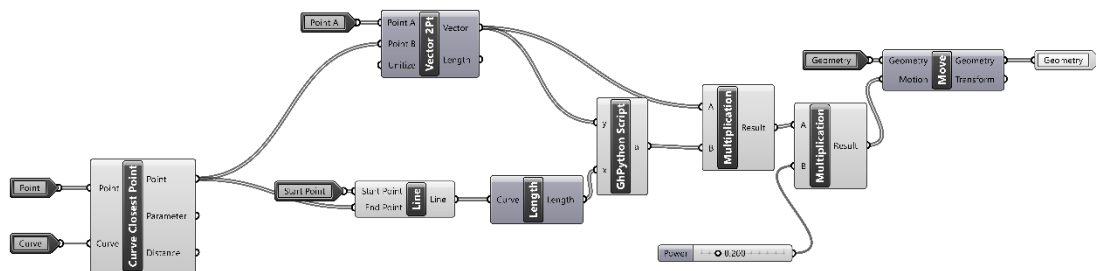


Figure 8: Pushing the Voronoi cells to edges and optimizing the final weight – “Modified distribution” cluster.

Inside the loop function, using the three concepts of creating Voronoi, using Lloyd’s algorithm, and pushing the cells to the edges – as shown in Figure 2 –, was resulted to present the final design of Voronoi tessellations. Figure 9 shows different distributions within different iteration to demonstrate the optimization of the modelling until

reaching the convergence state. Finally, the final surface design for the Voronoi tessellations is reported in Figure 10.

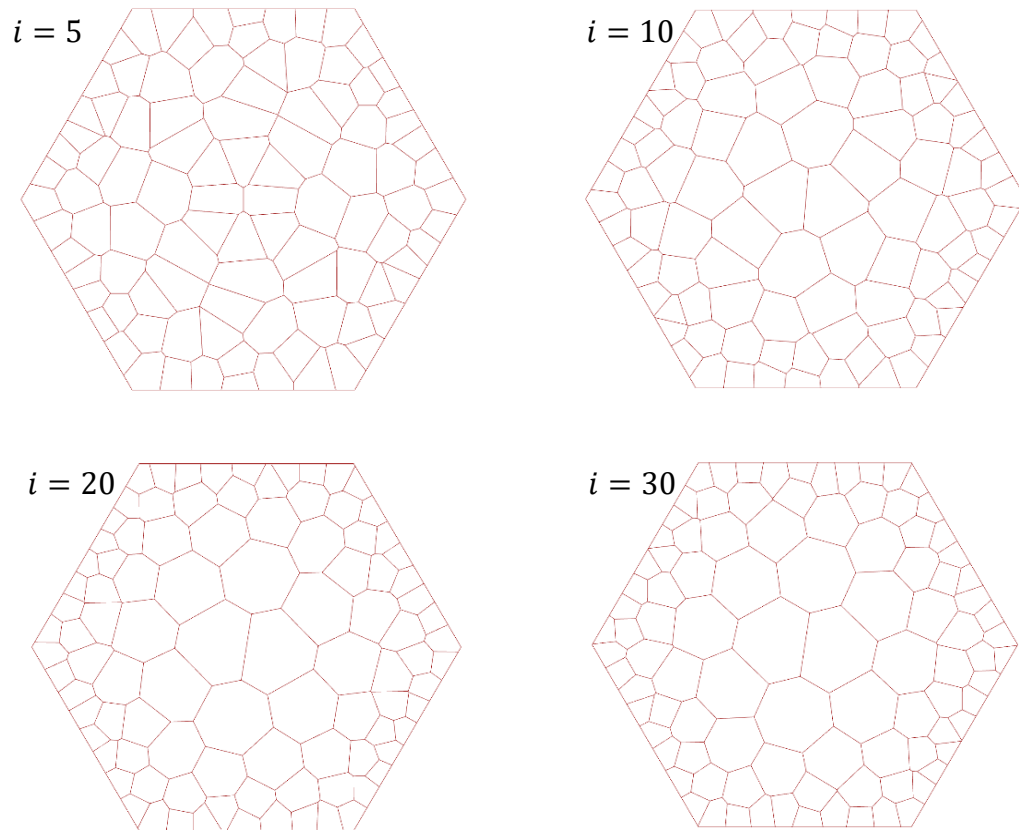


Figure 9: The Voronoi cells distribution in different number iterations shows almost the loop function's convergence.

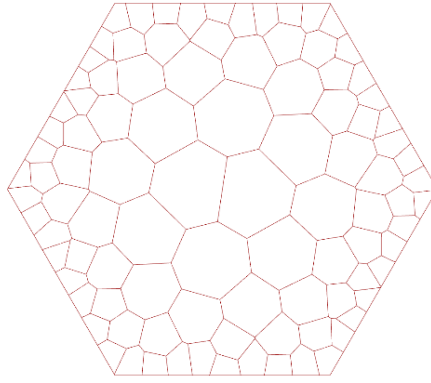


Figure 10: The Voronoi tessellation's final design is used later to fill the hexagonal honeycomb.

3D Model of the Hexagonal Honeycomb

The 3D model of the parametric design has been obtained to fit the allowable dimension for a fixed space that would be used to place an interior portion while considering the maximum allowed height for the 3D printer. Figure 11 shows the 3D model of the final design of hexagonal honeycomb filled with Voronoi tessellations.

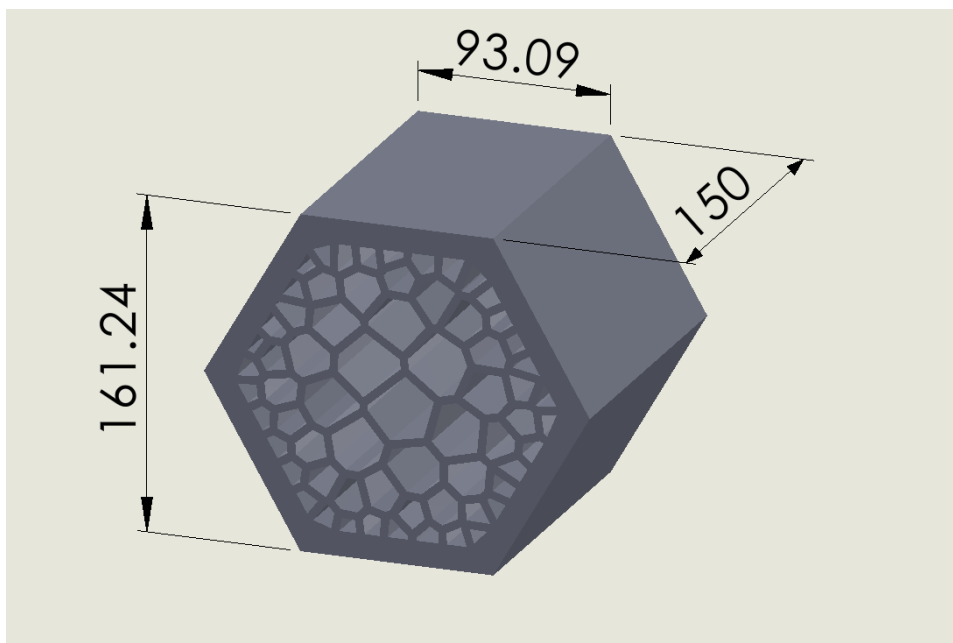


Figure 11: 3D model of the presented hexagonal honeycomb with the dimensions [mm].

Magnetic Convention

As discussed earlier, this design (Figure 11) would be used to build an interior partition through repeated patterns. Thus, magnetic coupling has been used to attach the hexagonal honeycomb. The design of the magnets coupling method is to make each hexagonal block to be attached with the other three blocks, using the very strong N52 neodymium magnets. Moreover, the reason for using those magnets is that the design would be used in a static application, and the blocks should be held with each other with extreme strength, so the whole partition structure becomes almost one unit. Three rectangular slots have been designed on the front surface disrupted near edges – as seen in Figure 12 – and those will be used to fit the magnets inside them. Those slots are very important in this study, and they will be called magnet slots. Another three magnet slots have been used on the rear side of the block to add more strength and higher stability. Hence, each block would have a total of 6 slots. Moreover, the slots have been designed to fit the supplied N52 magnets. The dimensions of the slots are $52 \times 52 \times 7 \text{ mm}$, which snugly fits with the selected magnets.

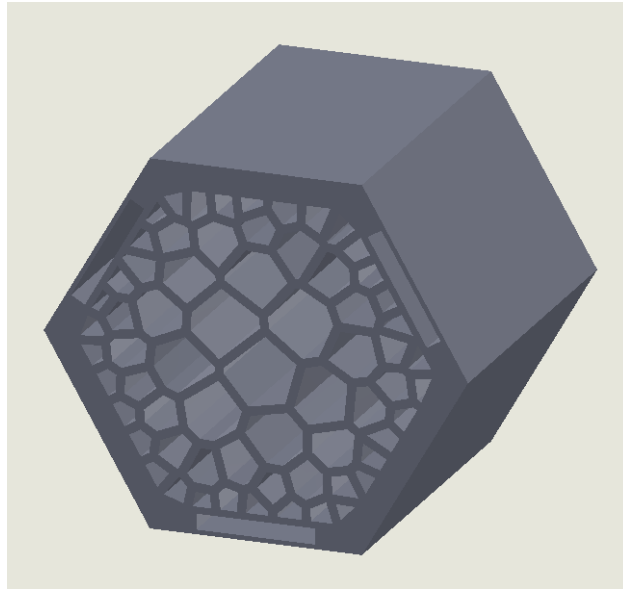


Figure 12: 3D model of the presented hexagonal honeycomb after including the magnet slots.

Magnets have been arranged in some pattern to enable the attraction between all magnets. Figure 13 shows the arrangement of the front, rear and internal coupling. For example, on the front side, the first row contains all N-blocks, which means that the north pole of the inserted magnet is directed to the outer surface, while the second row includes all S-blocks. Additionally, having opposite poles will ensure strong attraction and cohesion between the whole parts. Moreover, as shown in Figure 13, the arrangement of the rear coupling is precisely the opposite arrangement of the front one. These arrangements are intended to allow internal coupling, which ensures the attraction force between the front and rear magnets. Additionally, this attraction will ensure that the magnets are fixed and attracted to their slots without the need for any external setup.

To sum up, this subsection is essential to introduce the magnet slots, which would be used later in the analysis of the conducted tests.

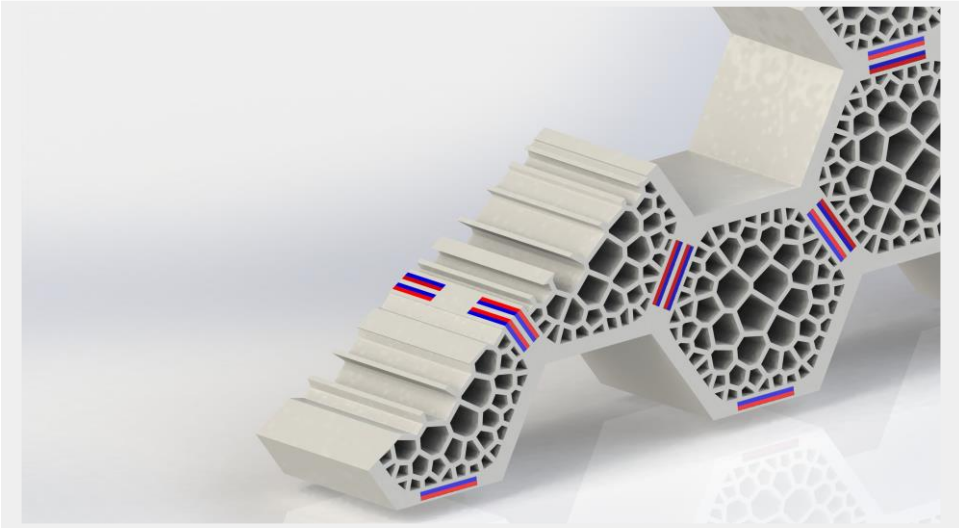
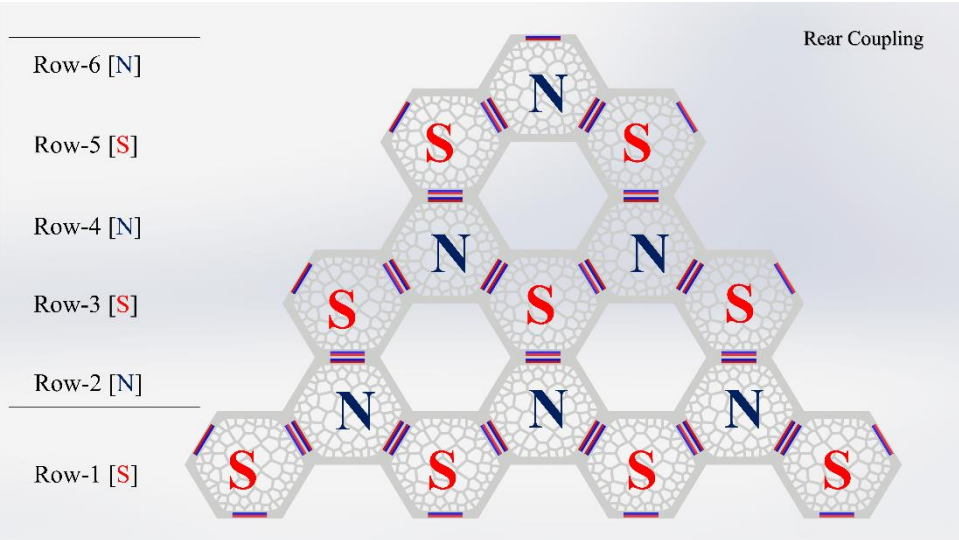
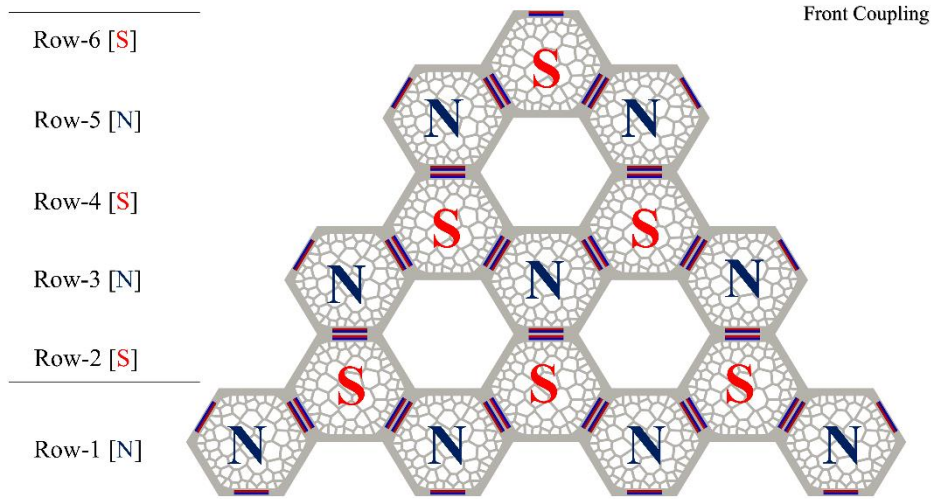


Figure 13: The arrangement of the front, rear and internal coupling, respectively, as the letter (N) and blue colour refer to the north pole of the magnet while the letter (S) and red colour refer to the south pole.

3D Printing

The final 3D model of the hexagonal honeycomb is shown in Figure 12. After having the 3D model file, the STL file should be exported. Then, slicing of the 3D model and developing a G-code for the 3D printer to follow based on the given STL file, using Cura software (shown in Figure 14).

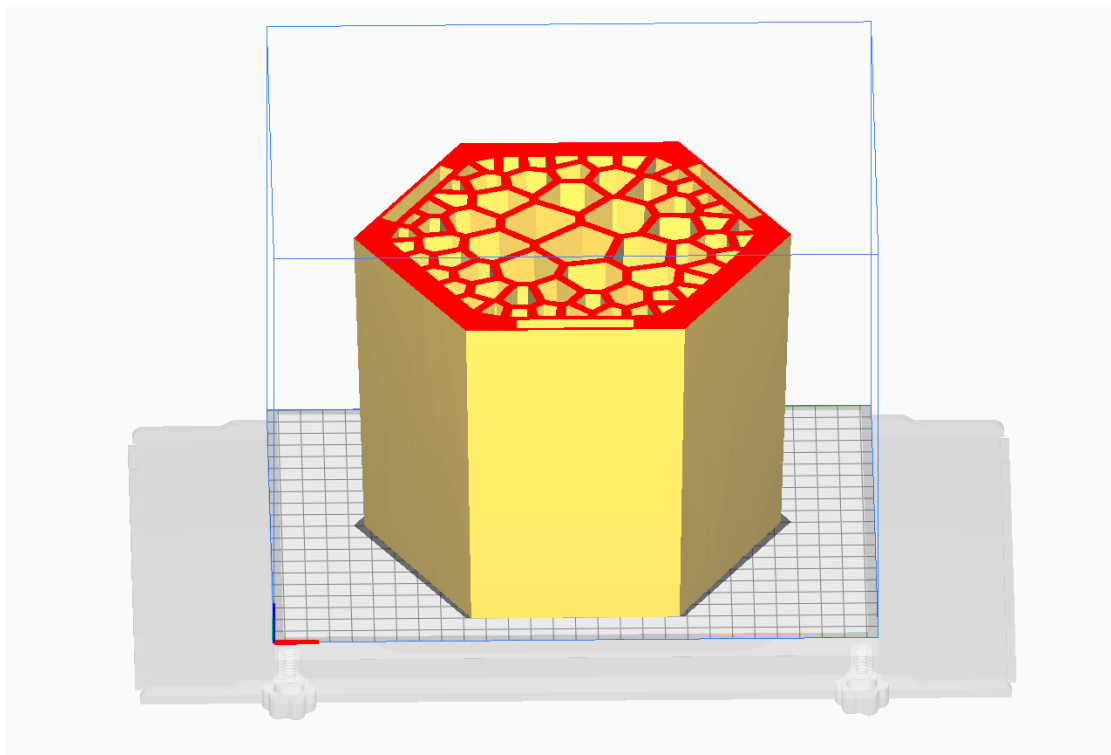


Figure 14: Snapshot of the interface of Cura software.

Moreover, the prototype is additively manufactured using through FDM process with a QIDI 3D X-Plus 3D printer. The advantage of this printer is that it has a quite big volume for printing, which fits the proposed design.

The settings of the 3D printing are mentioned in Table 2. The selection of those parameters was based on optimization of the cost and time required for printing while keeping the minimum enough strength, as the required application is static (only the weight is affecting). Moreover, the size of the final prototype was considered to be

relatively big, which means consuming more material and more time. Hence based on the literature review, and some trials and errors on a small prototype, those parameters have been selected. Furthermore, it is important to mention that an infill density of 10 % only would consume about 786 g and 39 hours based on Cura calculation, so this explains the need for optimizing cost and time. Because of the considerable material consumption, PolyLactic Acid-PLA (produced by HATCHBOX, China) is selected to be the printing material, as it is efficient for prototyping and cost. Moreover, different 3D printing settings have been tried in smaller prototypes to check the final quality during the trials and errors until reaching the settings that provided the enough amount of strength and printing quality as well. Some of those printed samples reported in Appendix 3. Table 3 shows the general PLA properties, as reported in [53].

Table 2: Setting of the 3D printing process

Printing parameter	Settings
Layer height	0.3 mm
Infill pattern	Grid
Infill density	10%
Printing temperature	200 C
Build plate temperature	60 C
Print speed	60 mm/s

Table 3: Typical ranges of mechanical properties for PLA material [53].

Mechanical Properties	Settings
Tensile modulus of elasticity	2020 to 3550 <i>MPa</i>
Ultimate tensile strength	14 to 70 <i>MPa</i>
Yield strength	15.5 to 72 <i>MPa</i>
Tensile elongation break	0.5 to 9.2%
Specific gravity	1.24 to 1.26 <i>g/cm³</i>

Tensile Test

Preparation of Test's Specimens

There is no standardized tensile test method for the 3D printed or FDM printed polymers[54]. However, the standardized (ASTM D638 – 14) [55] was used as it is the most used standard test method for tensile testing of polymers; also, it is obvious in Table 1. Furthermore, there are five types of ASTM D638, but Type I is chosen for the specimen's shape and dimensions, as Type I is the preferred specimen [55] and most used, as seen in Table 1. Following the procedure of the mentioned standard, the tensile specimens have the common shape of a dog bone with specified dimensions, as seen in Figure 15.

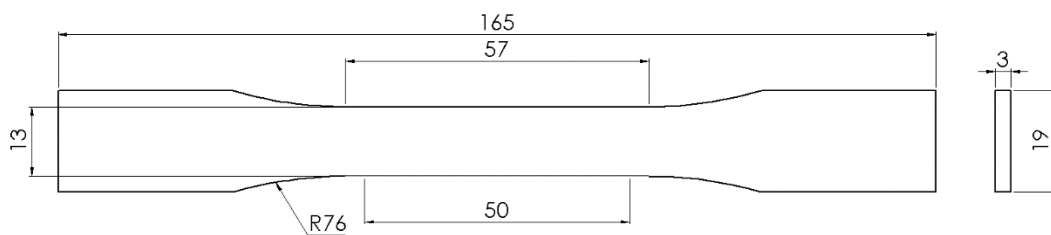


Figure 15: Geometrical data (in *mm*) of the dog bone specimen for the tensile test according to ASTM D638 – 14 (Type I).

Moreover, three test specimens were printed using the QIDI 3D printer – which was discussed earlier – with the same PLA material that has been used for the prototypes while following the same printing's settings mentioned in Table 2. A snapshot during the 3D printing process is shown in Figure 16, while Figure 17 shows the already printed specimens while specifying the gauge length ($L_0 = 50 \text{ mm}$) which is required to calculate the strain. The gauge length is determined by the ASTM D638 – 14 (Type I), as shown in Figure 15.

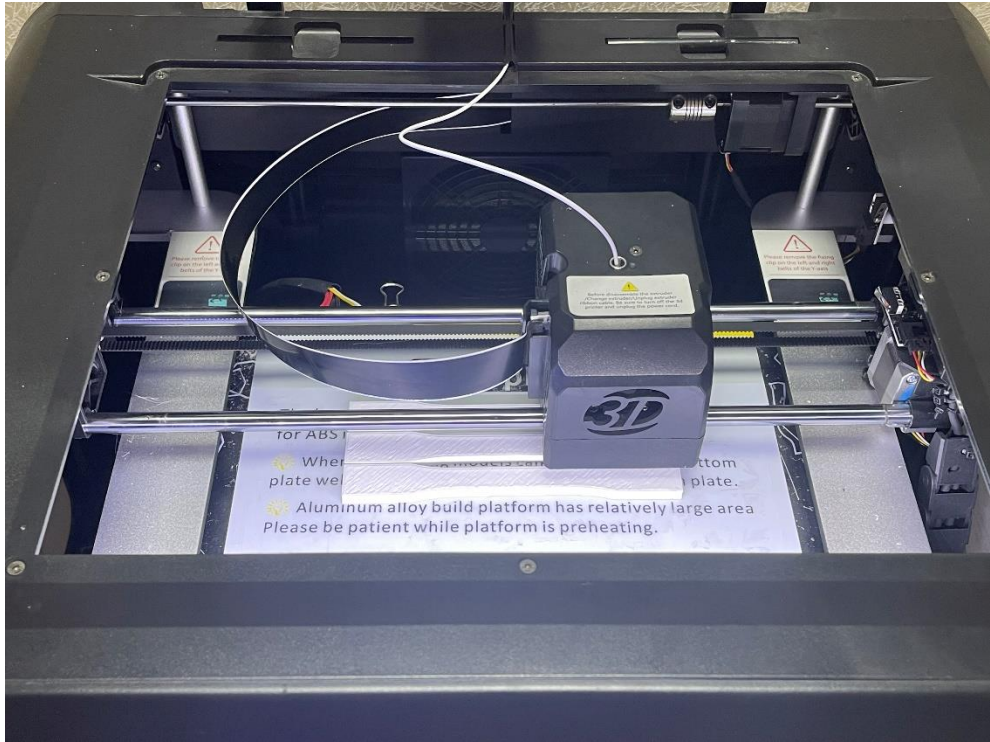


Figure 16: 3D printing the test specimens.

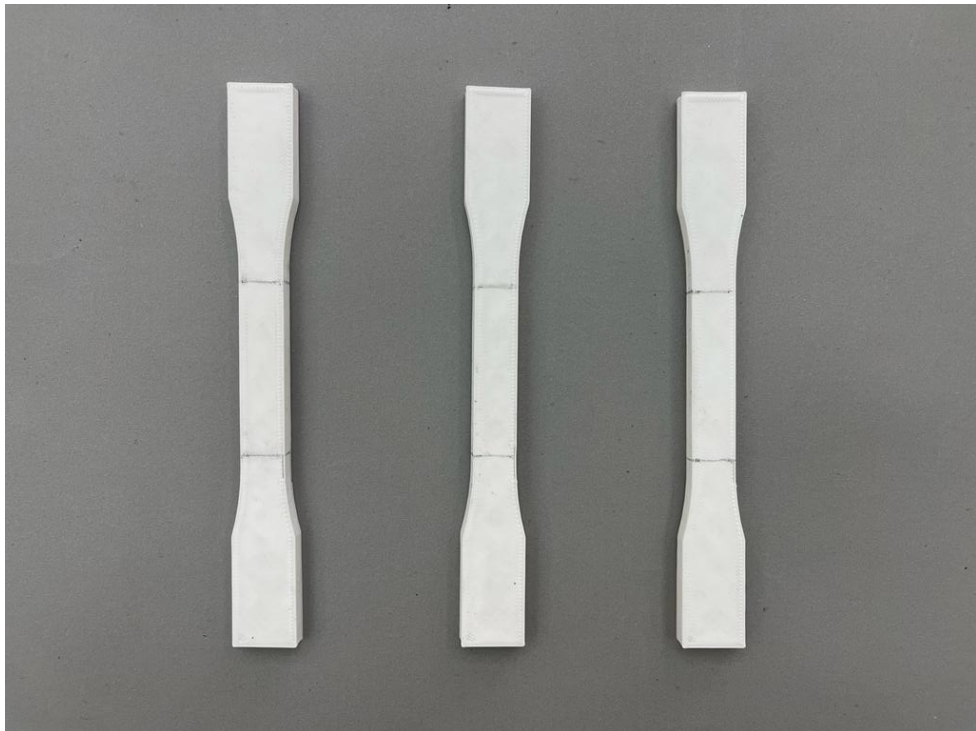


Figure 17: 3D printed tensile test's specimens.

Furthermore, the weight of those printed samples is mentioned in Table 4.

Table 4: Weights of the tensile specimens.

Sample	Weight [g]
Sample 1	8.95
Sample 2	8.93
Sample 3	8.96
Mean	8.95
SD	0.015

Test setup

Additionally, the crosshead speed during the tensile test should be constant with a value of 5 mm/min , as suggested by the ASTM D638 – 14 testing standards. The tensile tests were performed with Instron 5585 (Instron Corporation, Norwood, MA, USA) universal testing machine, while the Instron data acquisition system recorded the data of the tensile load and displacement of the upper bar. Figure 18 shows the setup of the experiment.



Figure 18: Specimen positioned and ready to be tested

Test Parameters

There are some parameters that should be discussed which be calculated from the tensile testing results, such as stresses and strains, in order to plot the stress-strain curve and obtain the values of the ultimate tensile strength (σ_t) and the modulus of elasticity (E). Moreover, the expression of the stress (σ) and strain (ε) are as follows:

$$\sigma = \frac{F}{A} \quad (1)$$

$$\varepsilon = \frac{\Delta L}{L_0} \quad (2)$$

Where A is the cross-section area of the reduced section in the dog bone shape, and F is the applied recorded force. Moreover, ΔL is the recorded displacement while L_0 is the length of the reduced section in the dog bone specimens. L_0 is the gauge length with value of 50 mm , as discussed earlier and shown in Figure 15.

Energy absorption testing experimental setup

Preparation of Test's Specimens

The energy absorption will be investigated through in-plane compressive loading on the experimental samples under quasi-static axial compression. The presented hexagonal honeycomb, which is shown in Figure 12, consumes a lot of material and time, which make it difficult to use the whole part to be compressed. For instance, there should be 30 printed samples if this design with the same dimensions was used, it would require almost 49 days to finish the printing while using almost 49 kg of PLA. So, the presented hexagonal honeycomb has been divided into three parts, one without slot, and two with slots, as shown in Figure 19. Hence, that would result in two types of hexagonal honeycomb, in terms of the existence of slots, shown in Figure 20.

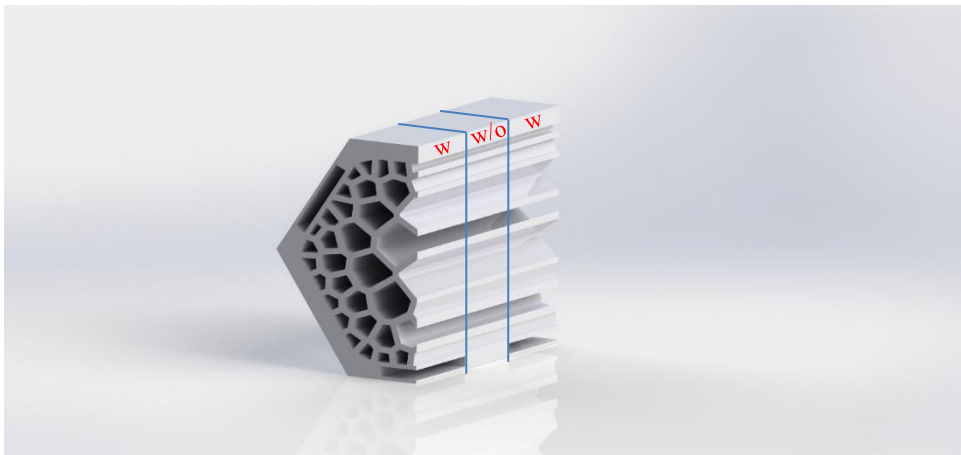


Figure 19: Dividing the proposed honeycomb to obtain the compression specimens. Where (w) refers to having slots, and (w/o) refers to not having ones.

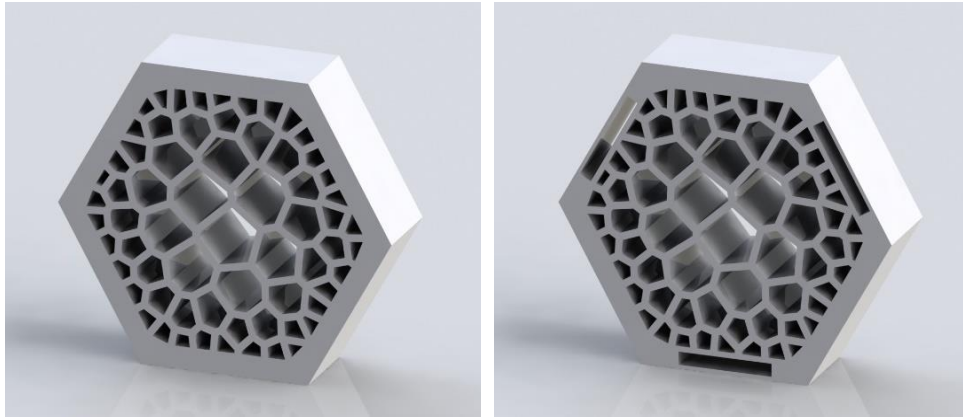


Figure 20: The two types of design for the compression specimens.

Hence, those designs mentioned in Figure 20 would be subjected to an in-plane compressive loading in order to investigate their energy absorption performance. Moreover, other designs are added to the testing to have a comparative investigation between the presented geometry and other different designs. Othman et al. [3] investigated the energy absorption capacity for four hexagonal honeycombs with various fillings – this study was discussed in Chapter 2 –. Moreover, their designs were on a small scale, with an infill density of 100%, different depths for each shape, and using ABS material. But in this presented investigation, those four shapes would be compared to the presented designs while printing them in PLA material, and with the same printing settings mentioned in Table 2 – only 10% of infill density –. Additionally, all the shapes have been designed to have the same outer thickness and the same depth, as shown in Figure 21. Those four shapes have been redesigned to have two designs from each shape, one with slots and the other without slots. Moreover, that would provide ten designs, five with slots and the other five without slots, while considering three samples for each design or configuration (Group). Table 5 shows the classifications and labeling for all samples.

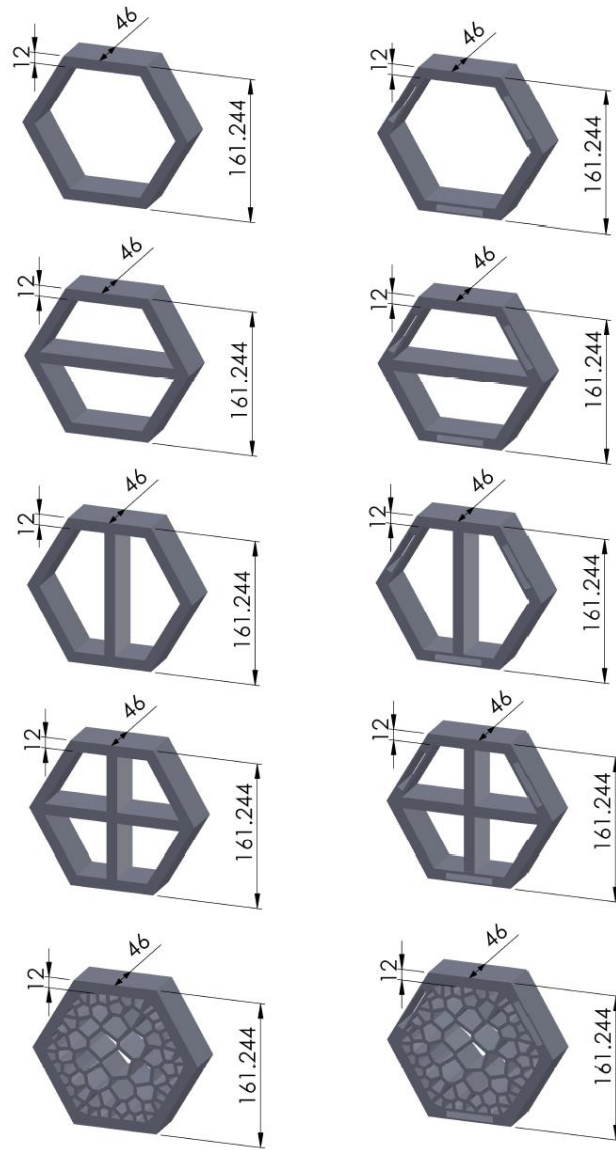
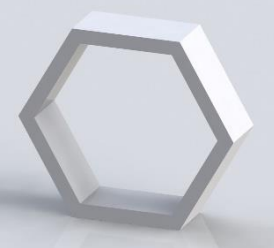
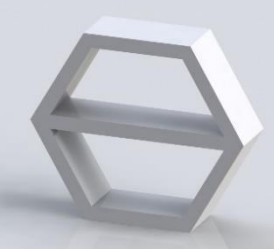
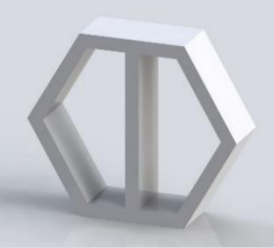
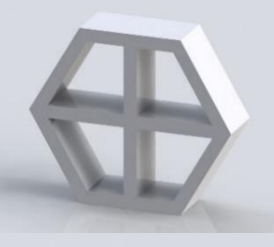
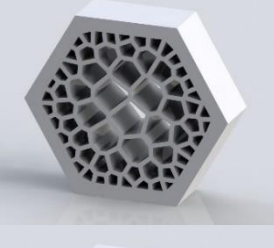



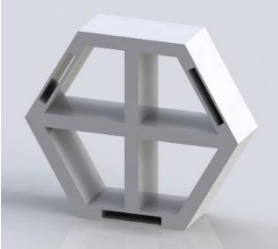
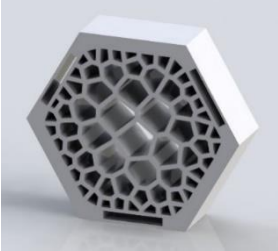


Figure 21: Geometrical data (in mm) of all compression test samples.

Table 5: Grouping and description of the experimental samples while showing the 3D models.

Description	Group #	3D Model	Name	Label
Hexagon with control shape – magnet slots are <u>excluded</u>	A		Control-w/o-1	A1
			Control-w/o-2	A2
			Control-w/o-3	A3
Hexagon with beam shape – magnet slots are <u>excluded</u>	B		Beam-w/o-1	B1
			Beam-w/o-2	B2
			Beam-w/o-3	B3
Hexagon with column shape – magnet slots are <u>excluded</u>	C		Column-w/o-1	C1
			Column-w/o-2	C2
			Column-w/o-3	C3
Hexagon with cross shape – magnet slots are <u>excluded</u>	D		Cross-w/o-1	D1
			Cross-w/o-2	D2
			Cross-w/o-3	D3
Hexagon with Voronoi shape – magnet slots are <u>excluded</u>	E		Voronoi-w/o-1	E1
			Voronoi-w/o-2	E2
			Voronoi-w/o-3	E3
Hexagon with control shape – magnet slots are <u>included</u>	F		Control-w-1	F1
			Control-w-2	F2
			Control-w-3	F3

Hexagon with beam shape – magnet slots are <u>included</u>	G		Beam-w-1	G1
			Beam-w-2	G2
			Beam-w-3	G3
Hexagon with column shape – magnet slots are <u>included</u>	H		Column-w-1	H1
			Column-w-2	H2
			Column-w-3	H3
Hexagon with cross shape – magnet slots are <u>included</u>	I		Cross-w-1	I1
			Cross-w-2	I2
			Cross-w-3	I3
Hexagon filled with Voronoi tessellation – magnet slots are <u>included</u>	J		Voronoi-w-1	J1
			Voronoi-w-2	J2
			Voronoi-w-3	J3

A total of thirty specimens were printed in PLA material using a QIDI 3D printer and following the same printing's settings mentioned in Table 2 in section. Furthermore, Figure 22 shows a 3D printed sample that is taken from each group. Moreover, the weights of all the 3D printed specimens are tabulated in Table 6.

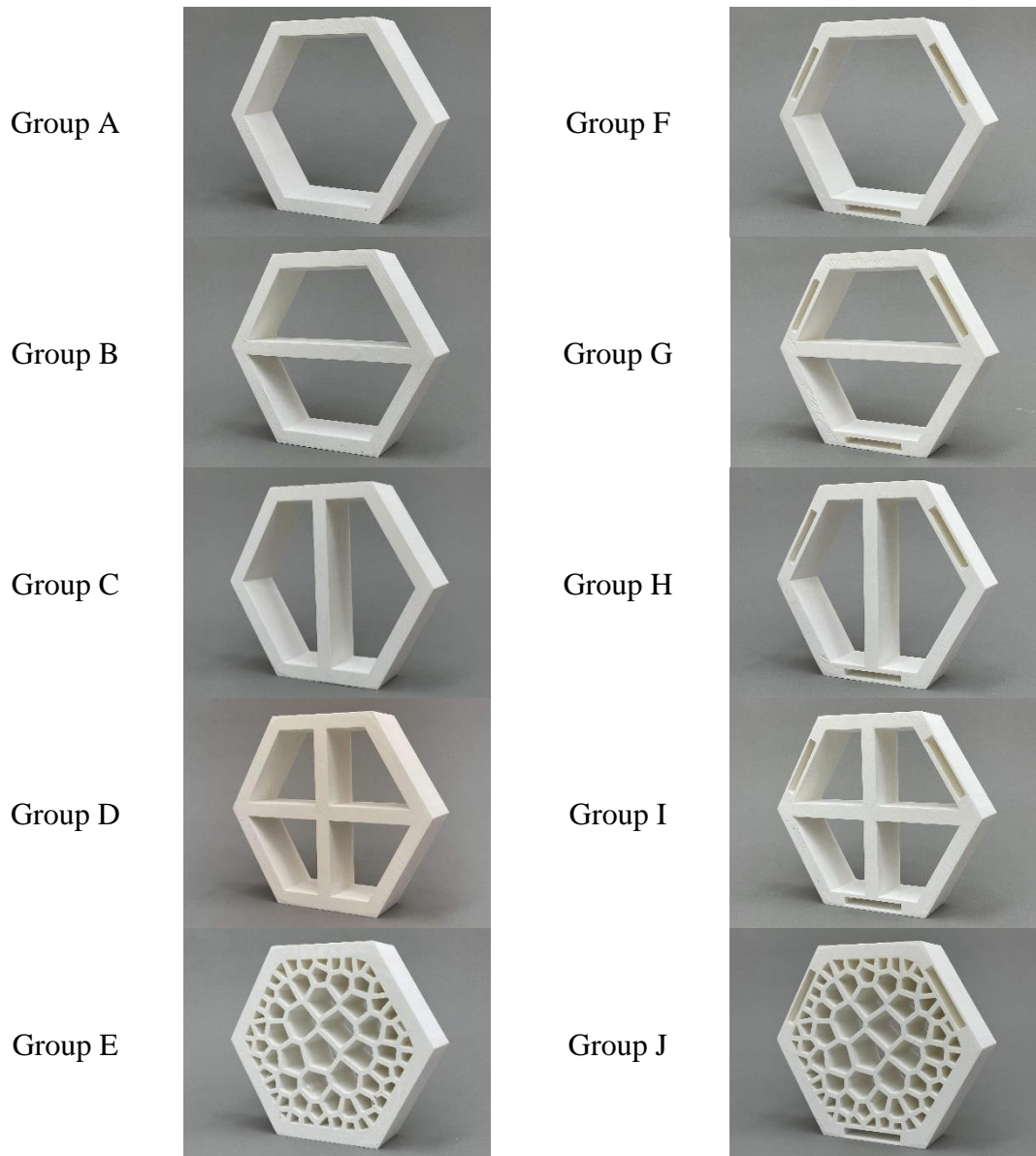


Figure 22: A 3D printed sample from each group.

Table 6: Weights of the compression specimens.

Groups	Weight [g]			Mean	SD
	Sample 1	Sample 2	Sample 3		
Group A	78.86	78.72	75.88	77.82	1.68
Group B	101.22	101.46	100.82	101.17	0.32
Group C	99.94	96.6	100.31	98.95	2.04
Group D	118.59	115.93	114.99	116.50	1.87
Group E	221.4	221.39	221.81	221.53	0.24
Group F	92.78	92.63	92.49	92.63	0.15
Group G	116.64	116.43	116.64	116.57	0.12
Group H	114.36	114.4	114.54	114.43	0.09
Group I	125.52	125.69	125.52	125.58	0.10
Group J	237.48	239.47	239.82	238.92	1.26

Test Setup

The proposed designs and configurations were subjected to in-plane compressive loading to investigate the performance of energy absorption characteristics and load-carrying capability. The in-plane compressive loading was conducted by the universal testing machine of Instron 5585 (Instron Corporation, Norwood, MA, USA) while following the ASTM E9-09 [56]. Moreover, the compression speed was fixed to be 15 *mm/min* [3]. Having three specimens for each configuration, as shown in Table 5, allowed having three tests for each different configuration to ensure data reproducibility. Furthermore, load-displacement data were recorded every one *ms* using the Instron data acquisition system. The crashing behavior of all designs and configurations was captured using video recording with a quality of 1080p HD at 60 frames per second.



Figure 23: The setup of the compression testing.

Energy Absorption Parameters

There are some parameters or indicators that should be discussed in order to have a correct investigation of the energy absorption characteristics. For instance, the total amount of absorbed energy is defined as the total area under the load and displacement curve, and it could be obtained by integrating the force-displacement curve until the initiation of the densification phase, as shown in Equation (3). The amount of absorbed energy could be calculated using MATLAB software by applying the function of $Trapz(x,y)$, where x is the recorded displacement (x) values and y is the recorded force (F) values. Moreover, the specific energy absorption (SEA) which indicates the amount of absorbed energy per unit mass (m), as shown in Equation (4) [57]. Furthermore, there are other essential indicators that play an important role in the energy absorption capacity and load carrying capabilities, such as the initial peak force (IPF) and crush force efficiency (CFE). The IPF indicates the amount of load required to allow the initiation of the permanent deformation, which could be obtained by getting the maximum force value in the force-displacement curve during the initial period [3]. Additionally, CFE mostly indicates the stability of the structure while carrying the applied load throughout the compression process, and it is calculated using Equation (5). Overall, those values are obtained to have a full understanding of the conducted energy absorption investigation for the Voronoi tessellation design. For instance, obtaining the maximum force that the design could go before permanent deformation using the IPF, and if it is stable while carrying the load or not by the CFE.

$$Energy\ absorption = \int_0^x F dx \quad (3)$$

$$SEA = \frac{Energy\ absorption}{m} \quad (4)$$

$$CFE = \frac{IPF}{Average\ Force} \quad (5)$$

CHAPTER 4: RESULTS AND DISCUSSION

In this chapter, all the experimental results are reported through various tables, graphs, and figures, along with the results' discussion. Moreover, the final printed prototype will be reported and discussed.

3D Printed Prototype

In this section, a prototype for the interior partition will be presented, which is consisting of 15 parts of the same hexagonal honeycomb in a repeated hierarchy pattern. So, using the printing procedure mentioned in Chapter 2 and printing settings mentioned in Table 2, 15 parts were printed to form the interior partition, attached with N52 neodymium magnets, as shown in Figure 24. However, this section is just to report the final prototype that was discussed earlier in Chapter 2 and to show the final application of the experimented hexagonal honeycomb. Additionally, the main discussion will be focused on the experimental tests, which will be discussed in the following section.

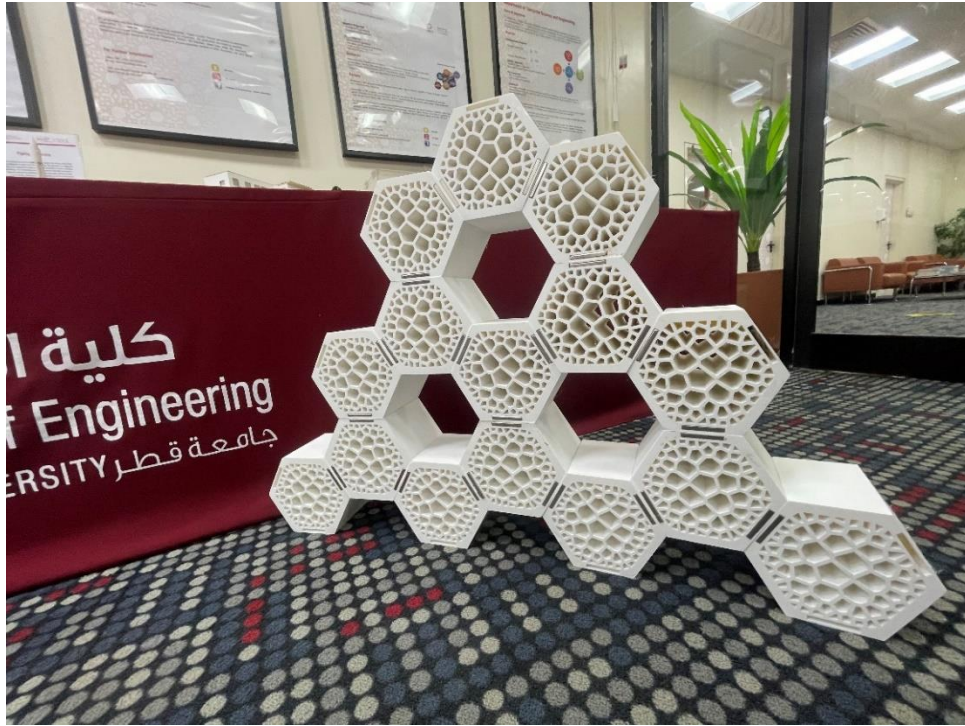


Figure 24: 3D printed prototype of the interior partition.



Figure 25: 3D printed prototype of the interior partition.

Results of Experimental Tests

Tensile Test Results

The tensile test was conducted to get some mechanical properties such as ultimate tensile strength and modulus of elasticity. All the performed tests were performed according to the standardized ASTM D638, as discussed earlier in Chapter 3. Figure 26 shows all the three broken test specimens after conducting the tensile test.

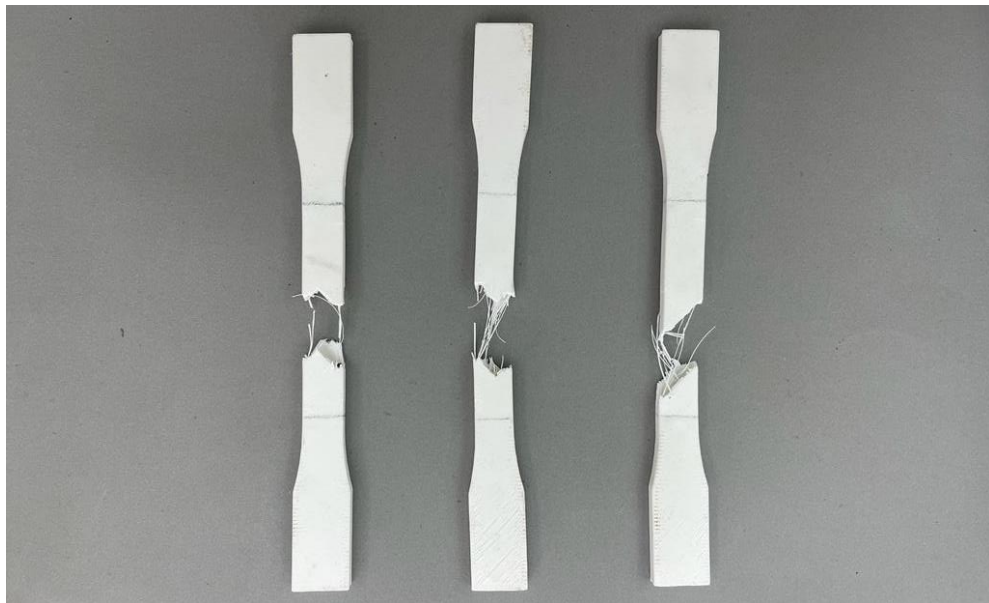


Figure 26: Test specimens after the tensile testing.

The stress-strain curves of the conducted tensile tests for the three specimens were obtained, as shown in Figure 27. Moreover, the values of stress (σ) in and non-dimensional strain (ϵ) were derived from the data recorded while conducting the test and through some calculations using Equation 1.

Using those graphs and values, the ultimate tensile strength (σ_t) is easy to be indicated at a specific strain (ϵ_t) as it is the maximum value reached by the stress in the stress-strain curve. The ultimate tensile strength (σ_t) is the maximum stress value in which the specimen is allowed to have before the breaking.

In addition, the graphs in Figure 28 are very useful to calculate the young modulus or the modulus of elasticity (E) in $[MPa]$, as it is the coefficient between the stress and strain for the initial linear elastic region. In other words, it is the slope of the initial linear elastic region. Additionally, it can be calculated by taking the linear region in the stress-strain curve (Figure 27) in a separate graph, and then a linear regression should be taken place, then the slope of the regression equation would be the modulus of elasticity. In Figure 28, the regression line of the initial linear region of the stress-strain curve is represented as a dotted line while showing the regression equation for each sample.

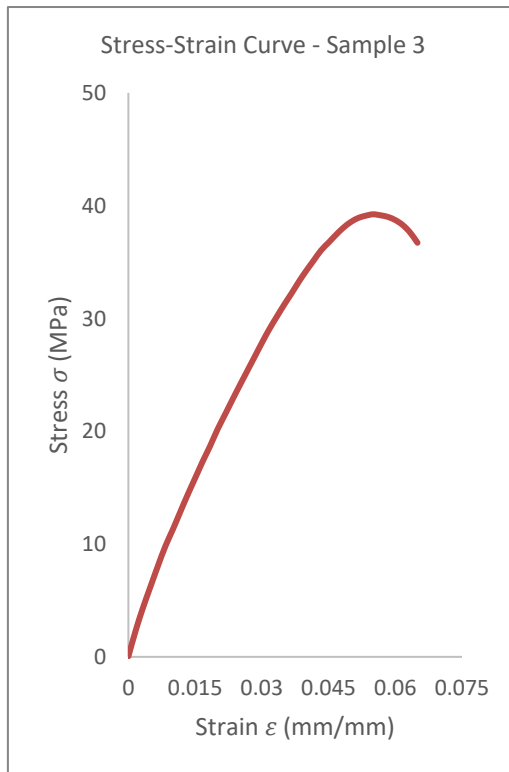
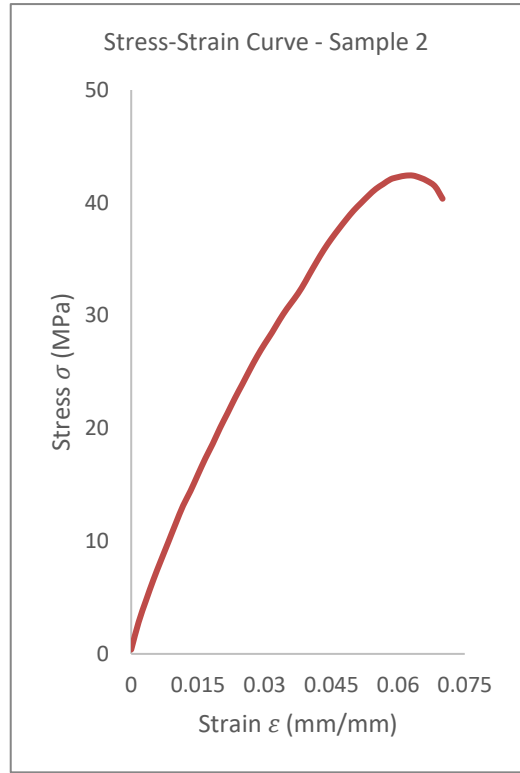
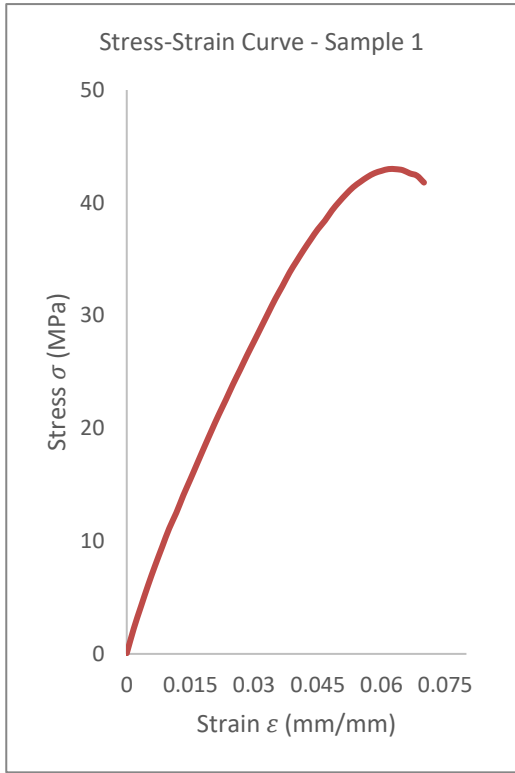


Figure 27: Stress-strain (σ - ϵ) tensile test curves for the three samples.

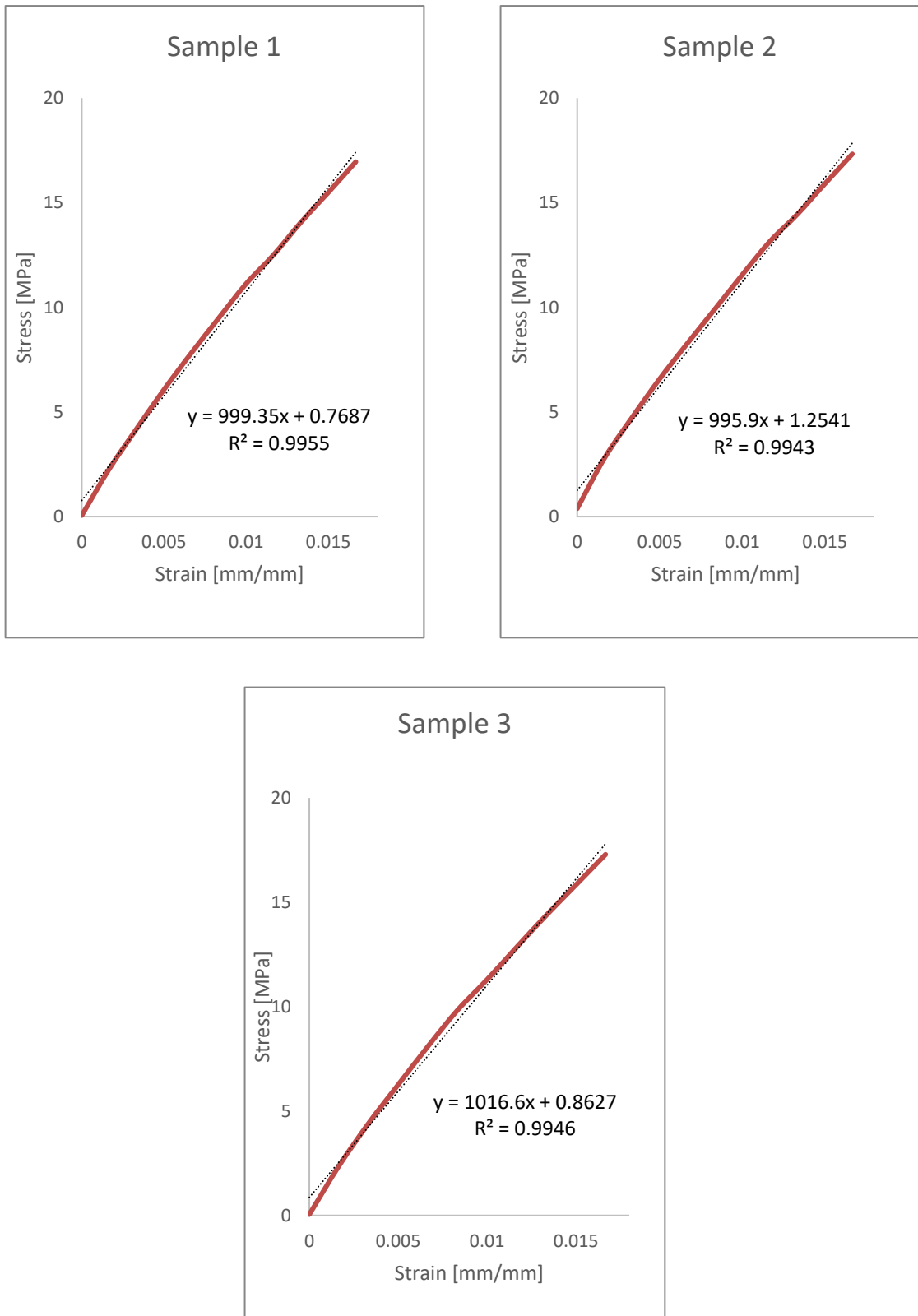


Figure 28: The regression line of the initial linear part of the stress–strain curve, is represented as dotted line, which is used for the calculation of E.

Moreover, the coefficient of determination (R^2) is obtained for each regression model as seen in Figure 28, and its values show that the initial elastic data is well-fitting the linear regression model. For instance, sample 3 is giving R^2 value of 0.9946 or 99.46%, which means 99.46% of the data fit for the linear regression model. All R^2 values are high (greater than 99%), which means a better fit for the conducted regression model.

Table 7: Tensile properties obtained from the conducted tensile tests.

	Ultimate Tensile Strength UTS (σ_t) [MPa]	Strain at σ_t (ϵ_t) $\left[\frac{mm}{mm}\right]$	Modulus of Elasticity (E) [MPa]
Sample 1	42.986	0.06167	999.35
Sample 2	42.411	0.06333	995.90
Sample 3	39.239	0.05500	1016.60
Mean	41.545	0.06000	1003.95
SD	2.0179	0.00441	11.0902

All of those discussed mechanical properties results are summarized and tabulated in Table 7. The first column sorts the tested specimens. The second, third and fourth columns present the ultimate tensile strength values, the corresponding strain (ultimate strain), and the modulus of elasticity, respectively, for each sample.

To sum up, in this section, Table 1 showed different experimental values of tensile results that are reported in various studies, and Table 3 showed the general theoretical tensile properties for PLA material. Moreover, the reported values for ultimate tensile strength is 41.545 ± 2.0179 [MPa] and for modulus of elasticity is 1003.92 ± 11.0902 [MPa], and both of them are within some of the reported ranges from the previously

discussed studies mentioned in both tables. The values are different because of the different 3D printing settings that are used in each study. Additionally, the presented values in this research – mentioned in Table 7 – are significantly important as there is a lack of research that investigated such a low infill percentage of 10%.

Energy Absorption Results

Ten geometries of honeycomb were crashed under quasi-static axial compression, five with magnet slots and another five without ones. Each configuration or geometry was presented – as discussed earlier in Chapter 2 – as one group, and each group consists of three same samples. Moreover, the results of the quasi-static axial compression experiment were the applied loadings (force) and displacements data that were recorded during the experiment. Those values were used to plot the force and displacement graph for each sample, and those graphs are reported in Figure 29 - Figure 38. Those graphs are very important to calculate and investigate other important parameters such as specific energy absorption (SEA), initial peak force (IPF), and crash force efficiency (CFE). Additionally, the crashing process and behaviour of all honeycomb samples with different configurations under quasi-static axial compression within different timeframes is presented in Appendix A (Table 11).

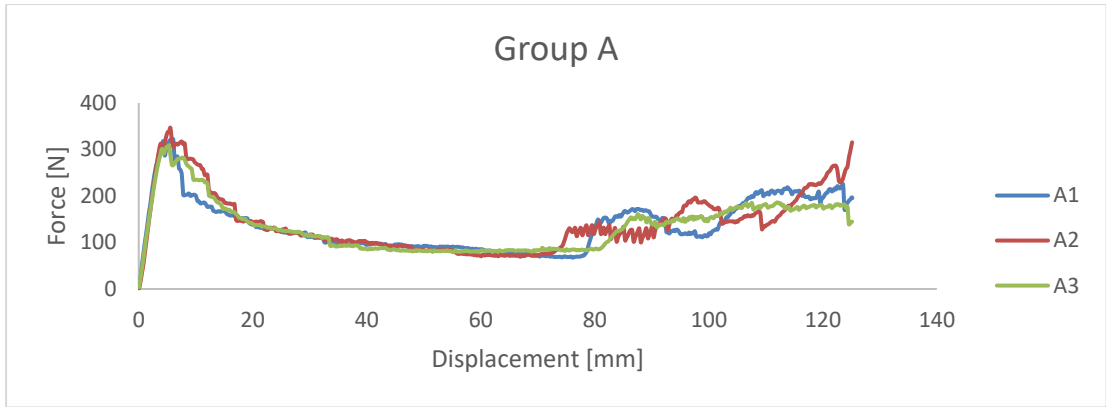


Figure 29: Force and displacement curves for Group A, honeycombs with Control configuration, slots are not included.

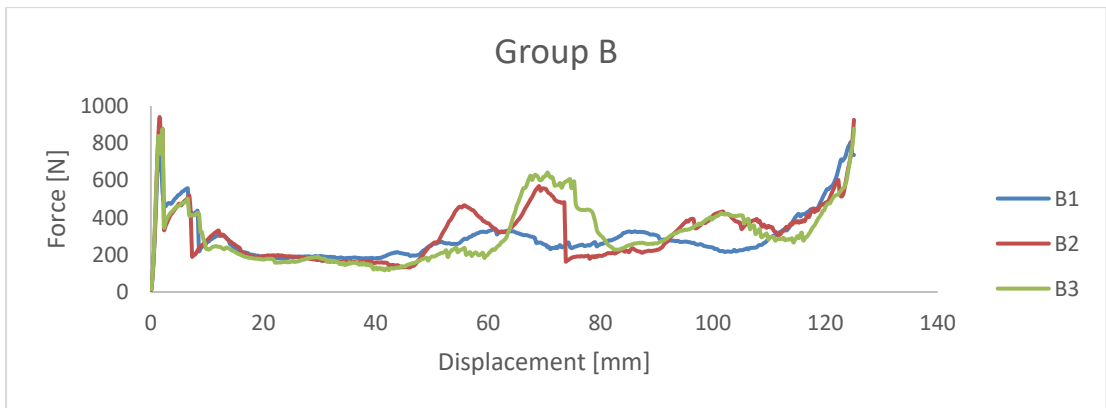


Figure 30: Force and displacement curves for Group B, honeycombs with Beam configuration, slots are not included.

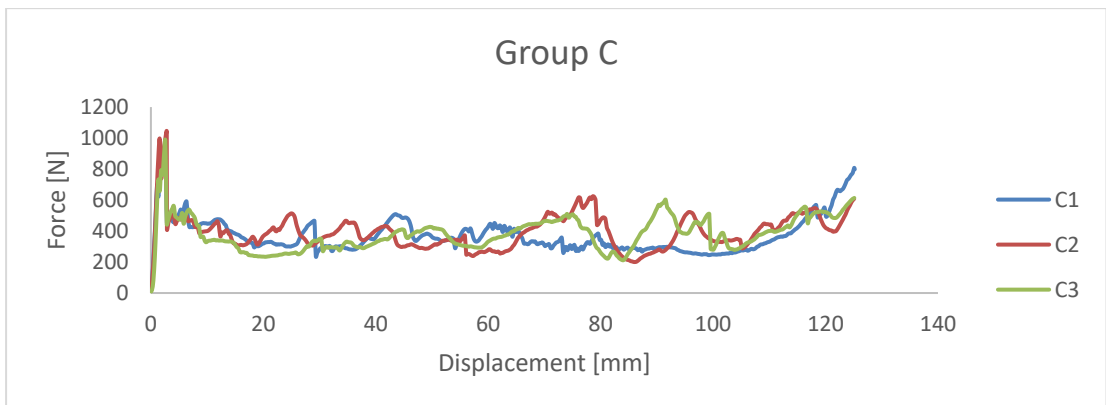


Figure 31: Force and displacement curves for Group C, honeycombs with Column configuration, slots are not included.

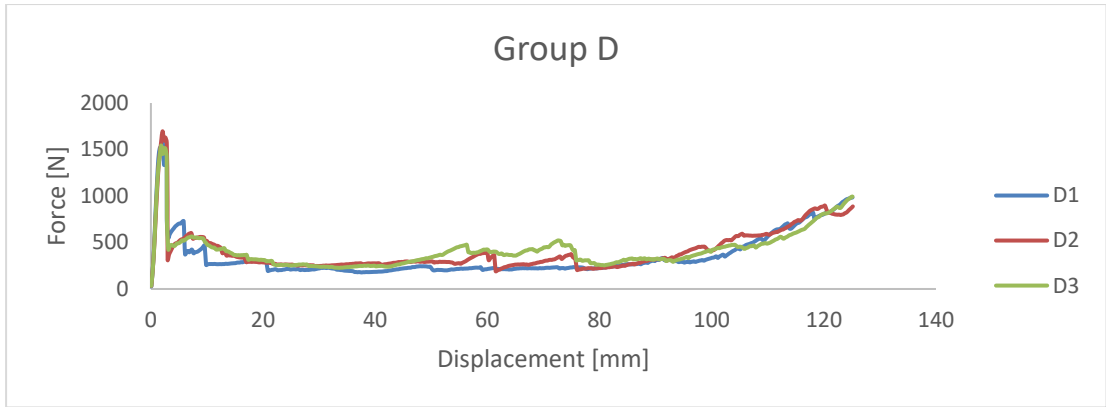


Figure 32: Force and displacement curves for Group D, honeycombs with Cross configuration, slots are not included.

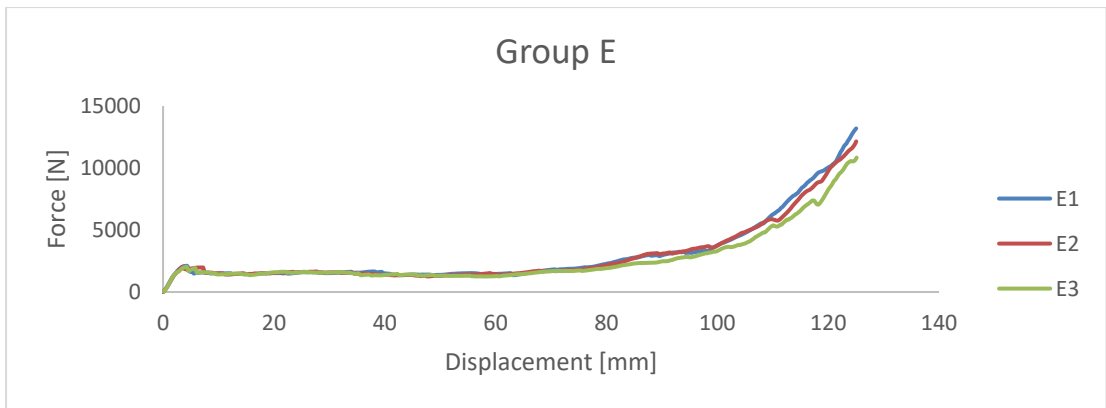


Figure 33: Force and displacement curves for Group E, honeycombs with Voronoi tessellation configuration, slots are not included.

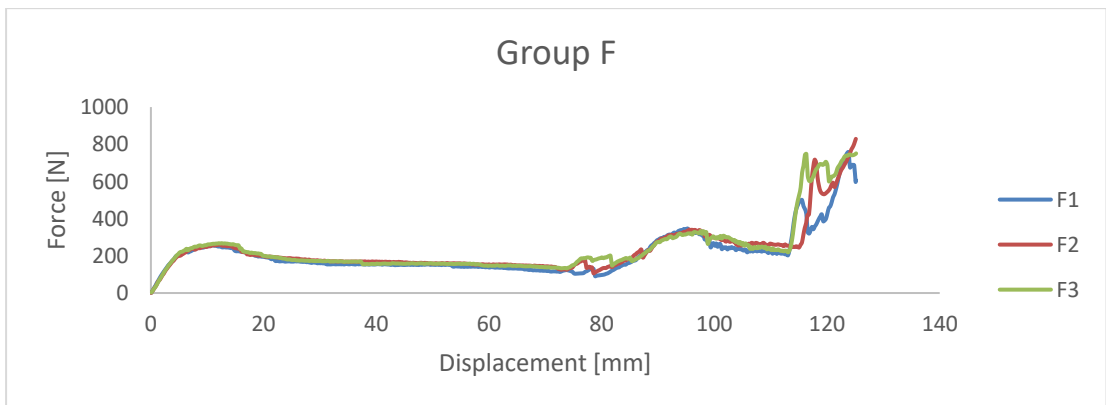


Figure 34: Force and displacement curves for Group F, honeycombs with Control configuration, slots are included.

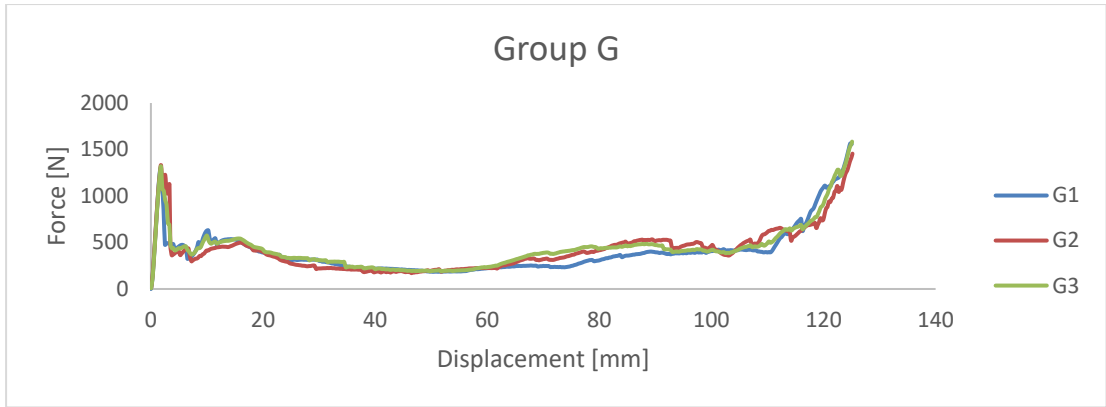


Figure 35: Force and displacement curves for Group G, honeycombs with Beam configuration, slots are included.

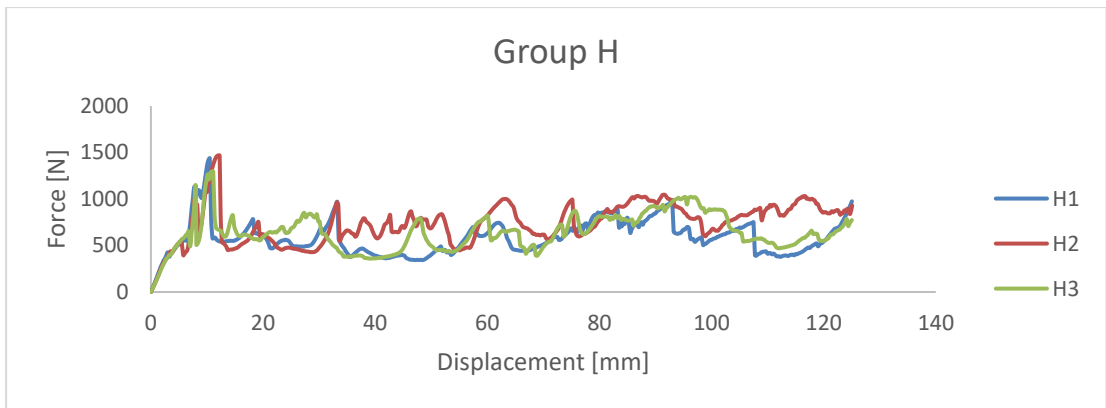


Figure 36: Force and displacement curves for Group H, honeycombs with Column configuration, slots are included.

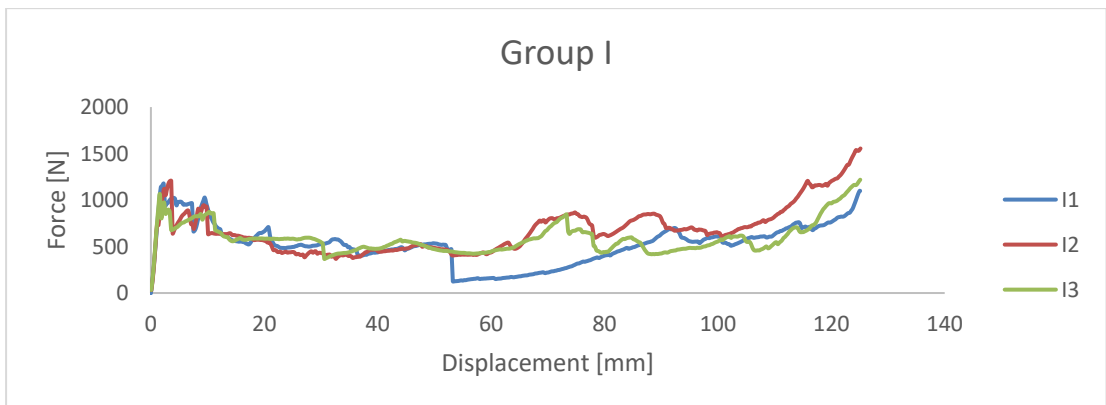


Figure 37: Force and displacement curves for Group I, honeycombs with Cross configuration, slots are included.

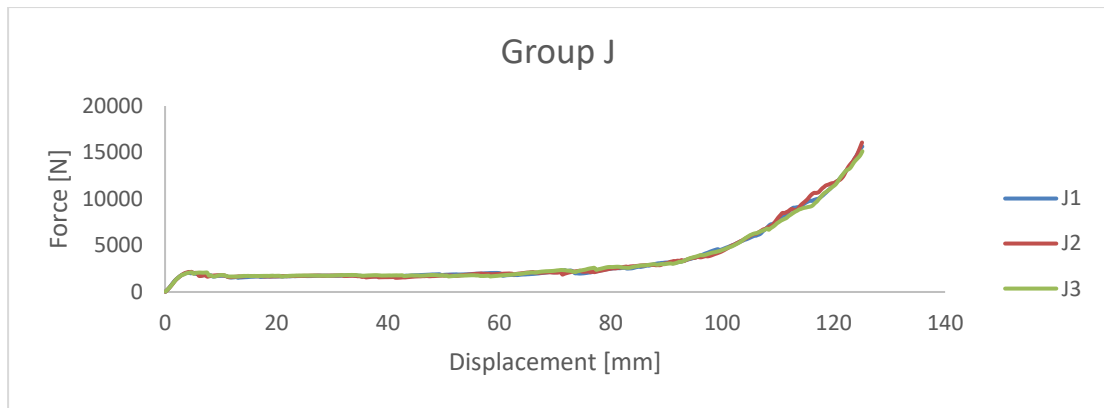


Figure 38: Force and displacement curves for Group J, honeycombs with Voronoi tessellations, slots are included.

As discussed in Chapters 2 and 3, the energy absorption is the area under the force and displacement curve. So, using the previous graphs and the MATLAB software as mentioned in Chapter 3, the values of the energy absorption values have been obtained. Table 8 summarizes the amount of absorbed energy for each group and each sample while reporting the calculated values of specific energy absorption (SEA). SEA was calculated using Equation (4). Moreover, it seems that the honeycombs with Voronoi tessellations (Group J and E) had the highest energy absorption capacities as they got the highest absorbed energy among the configurations with slots and the ones without slots. However, Group J has higher energy absorption than Group E because of the existence of slots in Group J, which increase the weight and the stress concentration in one of the slot's corners – as shown in Figure 41-. Those values and their influence on the existence of slots were discussed in more detail later within this chapter. Additionally, it seems that the coreless configuration (Group A and F) had the lowest energy absorption in both with/without slots designs. Furthermore, the column (Group C) and cross (Group D) configurations without slots design have very close values for the mean absorbed energy. While including slots allows the column configuration (Group H) to have higher mean absorbed energy than the cross one (Group I). However,

Group I has a higher value of weight (Table 6).

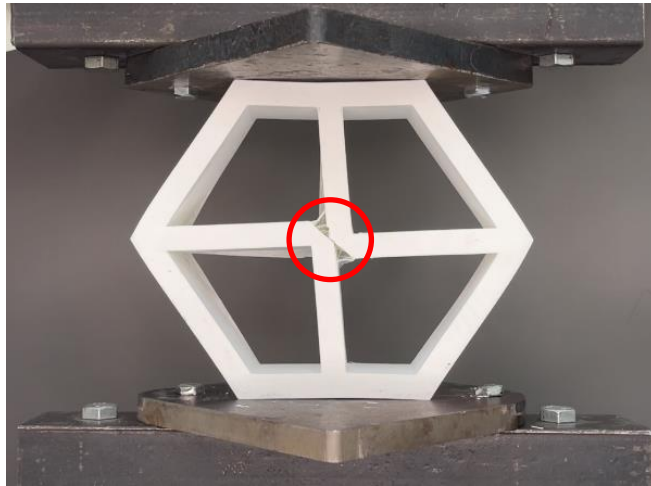


Figure 39: A snapshot of the crushing process of one sample from Group D.

Moreover, the values of SEA has almost the behaviour of absorbed energy values. However, the column shape (Group C and H) had higher SEA values than the weightier cross configuration (Group D and I) in both slots/without slots design. This unexpected behaviour of cross configuration could be explained by its crushing behaviour reported in Table 11. As there is a stress concentration which is located in the middle intersection as shown in Figure 39: then it breaks in the early beginning of the crushing process, as shown in Table 11.

Table 8: Experimental energy absorption results for each sample and the mean SEA for each group.

Groups	Energy Absorption [J]					Specific Energy Absorption [J/g]	
	Sample 1	Sample 2	Sample 3	Mean	SD	Mean	SD
Group A	17.214	17.820	16.833	17.289	0.498	0.222	0.008
Group B	36.392	39.018	38.563	37.991	1.404	0.376	0.014
Group C	46.357	49.414	47.763	47.845	1.530	0.484	0.018
Group D	44.199	50.854	52.163	49.072	4.271	0.421	0.037
Group E	372.960	362.495	325.877	353.777	24.722	1.597	0.112
Group F	26.453	28.593	29.865	28.304	1.724	0.306	0.019
Group G	49.847	51.835	60.828	54.170	5.851	0.465	0.050
Group H	73.096	92.172	80.214	81.828	9.640	0.715	0.084
Group I	65.952	84.705	73.685	74.781	9.424	0.595	0.075
Group J	434.417	436.040	433.585	434.681	1.249	1.819	0.011

Another indication for the energy absorption performances is the initial peak force (IPF), which is the highest applied force in the initial phase, as explained in Chapter 3. Moreover, Table 9 summarizes all the values of initial peak force for each sample while reporting the calculated mean and standard deviation values for each group. The honeycombs with Voronoi tessellations (Group E and J) have the highest IPF values among other configurations.

Table 9: Values of initial peak force for each sample, and the mean for each group.

Groups	Initial Peak Force [N]				
	Sample 1	Sample 2	Sample 3	Mean	SD
Group A	321.944	346.515	308.611	325.690	19.228
Group B	764.667	940.414	869.024	858.035	88.387
Group C	969.024	1041.683	979.816	996.841	39.208
Group D	1621.169	1696.419	1544.085	1620.558	76.169
Group E	2124.162	2023.870	2029.056	2059.029	56.466
Group F	256.950	259.661	268.061	261.557	5.793
Group G	1297.680	1329.063	1326.526	1317.756	17.433
Group H	1437.081	1469.414	1297.263	1401.253	91.497
Group I	1175.537	1206.617	1064.307	1148.820	74.822
Group J	2095.983	2165.273	2110.118	2123.791	36.613

As discussed earlier – in Chapter 3 – IPF values could be used to calculate the crashing force efficiency using Equation (5). Moreover, the average force and CFE values have been tabulated in Table 10. Again, Group E and J have the highest CFE values, indicating the honeycomb structure's stability filled with Voronoi tessellation in carrying the load throughout the compression process.

Table 10: The average of applied forces on every sample and the calculated mean of CFE.

Groups	Average Force [N]					Crash Force Efficiency (CFE)	
	Sample 1	Sample 2	Sample 3	Mean	SD	Mean	SD
Group A	142.737	137.564	134.488	138.263	4.169	0.425	0.028
Group B	291.923	313.489	309.536	304.983	11.482	0.355	0.039
Group C	371.079	395.647	382.204	382.977	12.302	0.384	0.020
Group D	356.336	408.036	394.700	386.357	26.841	0.238	0.020
Group E	3005.677	2919.139	2849.532	2924.783	78.225	1.420	0.054
Group F	212.334	229.953	239.734	227.340	13.885	0.869	0.056
Group G	401.713	415.653	489.161	435.509	46.984	0.330	0.036
Group H	585.076	736.841	641.312	654.409	76.725	0.467	0.063
Group I	528.060	678.763	590.480	599.101	75.720	0.521	0.074
Group J	3497.387	3516.656	3491.824	3501.956	13.031	1.649	0.029

Stress Analysis

In order to validate the claim of the increasing of stress concentration near the corners of the magnet slots in most of the configurations during the compression process, a simulation has been conducted on the Voronoi designs (Group E and J) only. So, the two designs have been simulated while applying an amount of load with values that are slightly less than the IPF, with the same experimental orientation using SolidWorks software. For instance, the applied force for Group J is 2000 N, and Group E is 1900 N. The values are not exactly the IPF to check the stress concentration before the permeant deformation. In order to have realistic results, the 3D models are redesigned with the same infill percentage and pattern instead of using an ordinary solid model, as shown in Figure 40. The meshing process has been conducted through the SolidWorks Mesher, Curvature based mesh, with a number of elements of 81270 for Group E and 83810 for Group J.

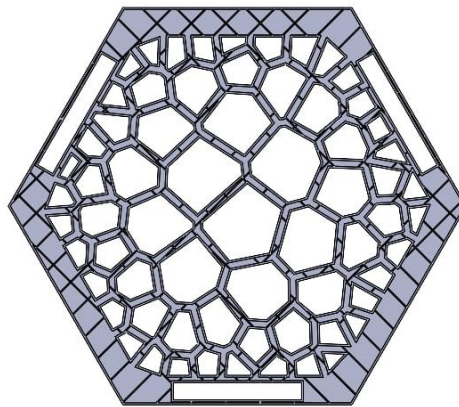


Figure 40: Section view of the 3D model used for simulation.

The design of Voronoi tessellations with slots included are investigated while applying the IPF value, which is mentioned in Table 9, to check the locations that have the highest stress concentration. As seen in Figure 41, the red regions show the regions

with high-stress concentration, which is mainly located in the corners of the magnet slots, edges, and the Voronoi cells. While in Figure 42, the contour plot shows fewer red regions because of the absence of the magnet slots.

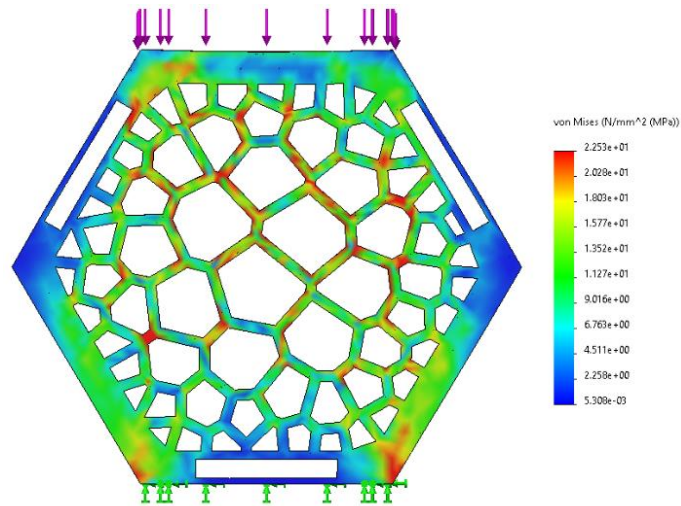


Figure 41: Contour plot that shows the stress concentrations in the front surface of Group J.

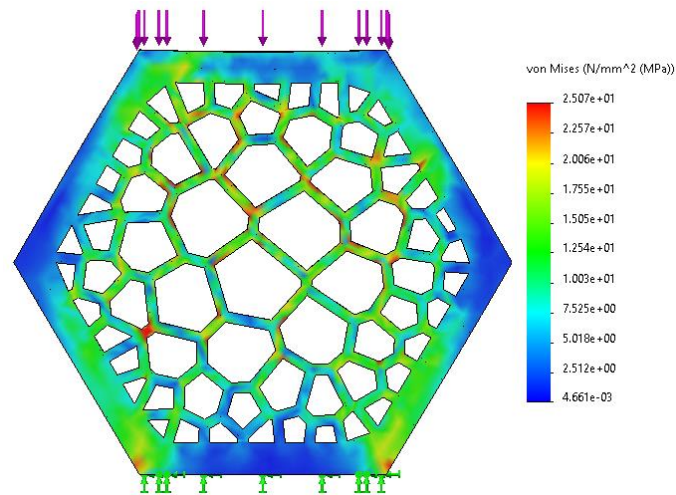


Figure 42: Contour plot that shows the stress concentrations in the front surface of Group E.

Energy Absorption Performance Discussion

As discussed before in Chapters 2 and 3, different parameters, along with the amount of absorbed energy such as SEA, IPF, and CFE, are essential to get a correct understanding of the energy absorption characteristics and performance. There are two types of the presented honeycomb structure that are investigated, one with three rectangular slots and one without any slot, as seen in Figure 21 and discussed in Chapter 3. Having those types allows us to have an interesting discussion about how the existence of those slots would affect the results.

As shown in Figure 43, Voronoi tessellation with slots design has almost more than four times cross and column designs. Moreover, the amount of absorbed energy for cross and column geometries is very close in both slots/without slots designs. As reported before, the column had a slightly higher value than cross design when the slots were included. Furthermore, Figure 43 shows a general trend that including slots in the geometries has significantly increased the amount of absorbed energy for all configurations comparing with the no slots designs.

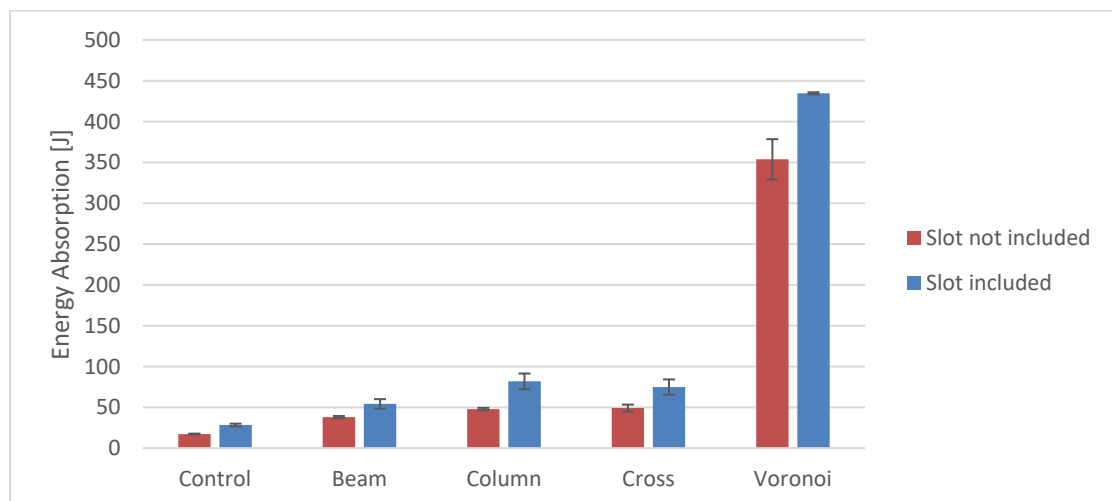


Figure 43: Bar charts summarizing the performance levels in terms of energy absorption.

It is not enough to discuss only the amount of absorbed energy, especially if the experimental specimens don't have similar weight, so SEA has been investigated as well and plotted, as shown in Figure 44. The previously mentioned general trend doesn't change as all the geometries with slots design has higher SEA than the same geometries but without slots. Although cross configurations have higher weight, it has less SEA value than column design which could be explained, as discussed in Figure 39. But, the existence of the slots allows the column configuration to has more than a 16% SEA increase than the cross one. Additionally, among the designs with slots, the Voronoi tessellation has more than the column configuration, which is the second-highest SEA value by 60% and by 70% for the designs without slots. Furthermore, the difference between the slots and without slots designs for Voronoi tessellation configuration is only 12%.

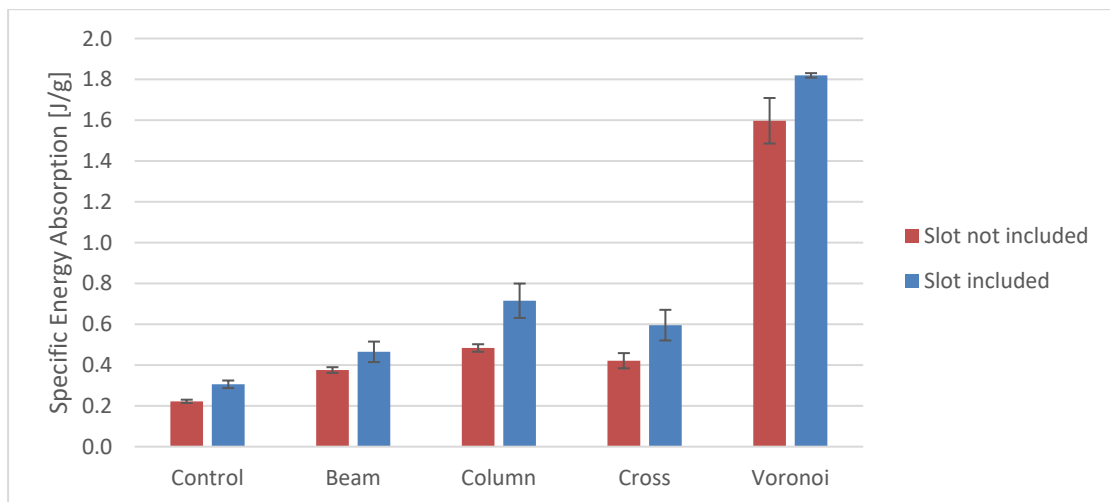


Figure 44: Bar charts summarizing the performance levels in terms of SEA.

Other important terms that their result should be discussed are IPF and CFE. As shown in Figure 46, The values of IPF for Voronoi tessellation are very close, with only a 3% difference. Moreover, the previously mentioned general trend cannot be reported here.

For instance, the cross configuration without slots design has significantly higher IPF than the one with slots included. The reason behind that is that adding slots in the cross shape would increase the stress concentration in at least one of the slots - as shown in Figure 41 - around slots' corners, and that would ease the crushing process. Hence, it would decrease the amount of load required to initiate a permanent deformation (crushing or breaking) in the structure, which means decreasing the IPF. This argument could be supported by the crushing process of Group I in Table 11. Additionally, among the designs without slots, the cross configuration has a higher value of IPF than column one, while the case is opposite when the SEA is discussed. This could be due to that during the compression process of the cross configuration, high force is required to overcome the intersection point (Figure 39) and then initiate the permanent deformation, and this initial required force is the IPF. After breaking this intersection point, there is not any other significant core support, which means less force would be required to continue the crushing process. Thus, the total area under the force-displacement curve would decrease, which means decreasing the energy absorption and SEA; see Figure 31 and Figure 32 for more clarification.

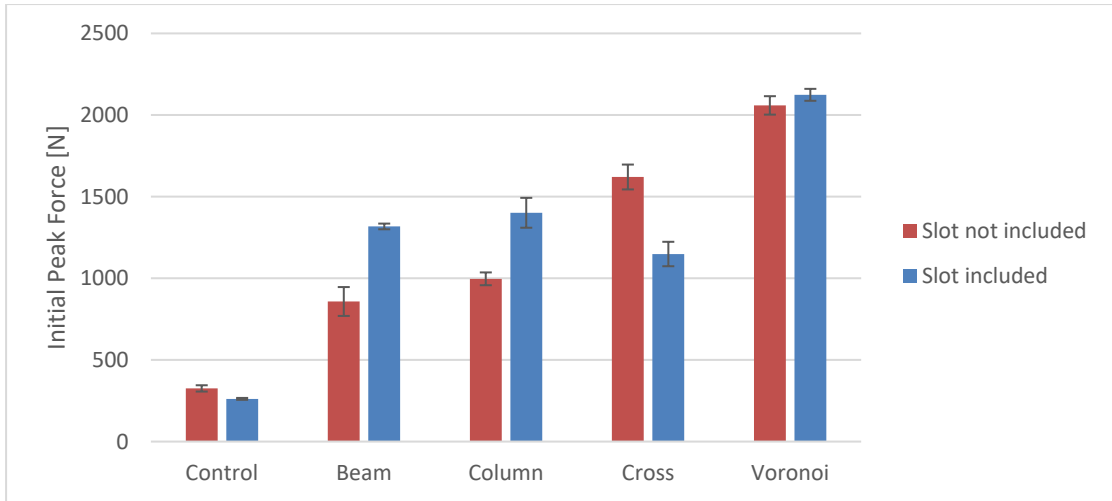


Figure 45: Bar charts summarizing the performance levels in terms of IPF.

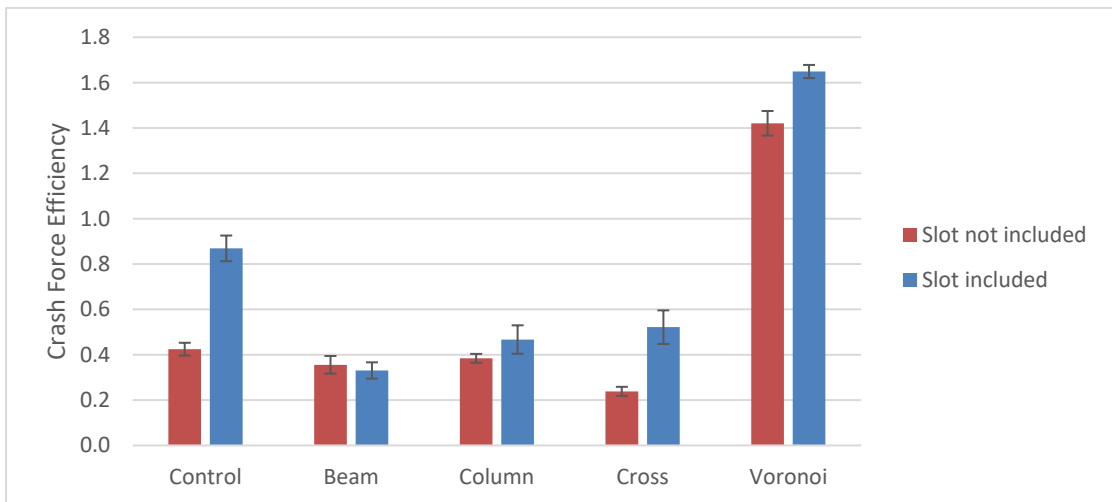


Figure 46: Bar charts summarizing the performance levels in terms of CFE.

Figure 46 shows a general trend of an increase in the CFE values for the designs with slots. However, the beam configuration with slots included has a slightly higher CFE than those without slots by only 7%. Moreover, the designs with slots and without slots, the coreless control configurations are the second-highest CFE, which reflects the structure's high stability in carrying the load during the compression process. Furthermore, among the designs with slots, the Voronoi tessellation has more than the control configuration, which is the second-highest CFE value by 47%, and 70% for the

designs without slots.

According to [3], among the cross, column, beam, and control configurations, the cross configuration has the highest IPF and SEA with the lowest CFE. But the coreless control had the highest CFE [3]. However, the presented Voronoi configuration has the highest SEA, IPF, and CFE. In other words, Laban (2021) could not obtain a design that has high energy absorption values while having high CFE, but the Voronoi design shows a very high CFE and a superior energy absorption performance.

CHAPTER 5: CONCLUSION, CONTRIBUTION OF KNOWLEDGE, AND FUTURE WORK

In conclusion, this thesis addresses a comparative investigation of energy absorption performance for hexagonal honeycombs with different infilling structures. Additionally, a tensile test has been conducted for the 3D printed PLA material to get the required tensile mechanical properties. Having a honeycomb filled with Voronoi tessellations showed the highest SEA, IPF, and CFE, while having slots in their design would increase their performance even more. Moreover, a discussion has been introduced which shows how the 3D printing parameters could affect the mechanical properties of the 3D printed material.

The contribution to the knowledge of this study could be listed as follows:

- 1) Investigating the energy absorption performance of a 3D printed Voronoi tessellation hexagonal honeycomb, in comparison with four internal topologies (i.e. cross, column, beam, and control designs) in Laban (2021),
- 2) Conducting a tensile test for 3D printed PLA where is a lack of actual results and research, based on the comprehensive literature reviews that were evaluated.
- 3) Using a very low infill percentage of 10% in both energy absorption and mechanical properties investigations, and there is almost no one addressed such infill percentage with those investigations.
- 4) Obtaining a high SEA and IPF design while maintaining high CFE as well, where Laban et al. (2021) failed to achieve.

Overall, this provides an aesthetic structure with very lightweight, which saves material and time while providing good energy absorption properties.

In addition, the best Voronoi structures also exhibit superior mechanical and energy

absorption properties compared to their non-Voronoi counterparts, with energy absorption values ranging from 350 J to 435 J and crash force efficiency being 1.42 to 1.65. It is noteworthy that all of the specimens and prototypes have been printed with an infill density of 10% only, which make these structures very lightweight and save material and money while providing good energy absorption properties.

In the future, the research could be expanded to cover the limitation of the design such as the slow printing time, layer delamination, and various material testing. This could be done using the parametric modelling method, more designs and tessellations could be investigated with different thicknesses. Moreover, doing the same investigating while having different material other than PLA or using different settings for the 3D printing process. For instance, investigating how the tensile and energy absorption results would differ if different infill patterns, materials, layer heights, or other 3D printing factors were used.

REFERENCES

- [1] P. Parandoush and D. Lin, “A review on additive manufacturing of polymer-fiber composites,” *Compos. Struct.*, vol. 182, pp. 36–53, 2017,
- [2] M. Dermentzi, “This 3D printed green wall comes with an embedded irrigation system - Tech,” 2019. <https://sea.mashable.com/tech/4886/this-3d-printed-green-wall-comes-with-an-embedded-irrigation-system> (accessed Oct. 06, 2021).
- [3] O. Laban, E. Mahdi, S. Samim, and J.-J. Cabibihan, “A Comparative Study between Polymer and Metal Additive Manufacturing Approaches in Investigating Stiffened Hexagonal Cells,” *Materials (Basel)*, vol. 14, no. 4, 2021,
- [4] C. W. Hull and C. Arcadia, “Apparatus for production of three-dimensional objects by stereolithography,” Aug. 1984.
- [5] D. T. Pham and S. S. Dimov, *Rapid Manufacturing*. London: Springer London, 2001.
- [6] S. Shipp *et al.*, “Emerging Global Trends in Advanced Manufacturing,” 2012.
- [7] C. Abeykoon, P. Sri-Amphorn, and A. Fernando, “Optimization of fused deposition modeling parameters for improved PLA and ABS 3D printed structures,” *Int. J. Light. Mater. Manuf.*, vol. 3, no. 3, pp. 284–297, 2020,
- [8] G. W. Melenka, B. K. O. Cheung, J. S. Schofield, M. R. Dawson, and J. P. Carey, “Evaluation and prediction of the tensile properties of continuous fiber-reinforced 3D printed structures,” *Compos. Struct.*, vol. 153, pp. 866–875, 2016,
- [9] E. Lepowsky and S. Tasoglu, “3D printing for drug manufacturing: A perspective on the future of pharmaceuticals,” *Int. J. bioprinting*, vol. 4, no. 1, p. 119, Sep. 2017,

- [10] J. I. Lipton, M. Cutler, F. Nigl, D. Cohen, and H. Lipson, “Additive manufacturing for the food industry,” *Trends Food Sci. Technol.*, vol. 43, no. 1, pp. 114–123, May 2015,
- [11] N. Guo and M. C. Leu, “Additive manufacturing: technology, applications and research needs,” *Front. Mech. Eng.*, vol. 8, no. 3, pp. 215–243, Sep. 2013,
- [12] X. Fu, X. Zhang, and Z. Huang, “Axial crushing of Nylon and Al/Nylon hybrid tubes by FDM 3D printing,” *Compos. Struct.*, vol. 256, p. 113055, Jan. 2021,
- [13] D. Popescu, A. Zapciu, C. Amza, F. Baci, and R. Marinescu, “FDM process parameters influence over the mechanical properties of polymer specimens: A review,” *Polym. Test.*, vol. 69, pp. 157–166, 2018,
- [14] C. Buchanan and L. Gardner, “Metal 3D printing in construction: A review of methods, research, applications, opportunities and challenges,” *Eng. Struct.*, vol. 180, pp. 332–348, Feb. 2019,
- [15] Y. W. D. Tay, B. Panda, S. C. Paul, N. A. Noor Mohamed, M. J. Tan, and K. F. Leong, “3D printing trends in building and construction industry: a review,” *Virtual Phys. Prototyp.*, vol. 12, no. 3, pp. 261–276, Jul. 2017,
- [16] N. Elmabet and P. Siegkas, “Dimensional considerations on the mechanical properties of 3D printed polymer parts,” *Polym. Test.*, vol. 90, p. 106656, 2020,
- [17] I. Gibson, D. Rosen, B. Stucker, and M. Khorasani, *Additive Manufacturing Technologies*. Cham: Springer International Publishing, 2021.
- [18] M. Pérez, D. Carou, E. Rubio, and R. Teti, “Current advances in additive manufacturing,” vol. 88, pp. 439–444, Jun. 2020,
- [19] T. Yao, Z. Deng, K. Zhang, and S. Li, “A method to predict the ultimate tensile strength of 3D printing polylactic acid (PLA) materials with different printing orientations,” *Compos. Part B Eng.*, vol. 163, pp. 393–402, Apr. 2019,

- [20] C. Casavola, A. Cazzato, V. Moramarco, and C. Pappalettere, “Orthotropic mechanical properties of fused deposition modelling parts described by classical laminate theory,” *Mater. Des.*, vol. 90, pp. 453–458, Jan. 2016,
- [21] N. Mohan, P. Senthil, S. Vinodh, and N. Jayanth, “A review on composite materials and process parameters optimisation for the fused deposition modelling process,” *Virtual Phys. Prototyp.*, vol. 12, no. 1, pp. 47–59, Jan. 2017,
- [22] R. Johnston and Z. Kazancı, “Analysis of additively manufactured (3D printed) dual-material auxetic structures under compression,” *Addit. Manuf.*, vol. 38, p. 101783, Feb. 2021,
- [23] F. A. Santos *et al.*, “Low velocity impact response of 3D printed structures formed by cellular metamaterials and stiffening plates: PLA vs. PETg,” *Compos. Struct.*, vol. 256, p. 113128, Jan. 2021,
- [24] M. Rismalia, S. C. Hidajat, I. G. R. Permana, B. Hadisujoto, M. Muslimin, and F. Triawan, “Infill pattern and density effects on the tensile properties of 3D printed PLA material,” *J. Phys. Conf. Ser.*, vol. 1402, p. 044041, Dec. 2019,
- [25] M. Q. Tanveer, A. Haleem, and M. Suhaib, “Effect of variable infill density on mechanical behaviour of 3-D printed PLA specimen: an experimental investigation,” *SN Appl. Sci.*, vol. 1, no. 12, p. 1701, Dec. 2019,
- [26] B. Abdullah Aloyaydi, S. Sivasankaran, and H. Rizk Ammar, “Influence of infill density on microstructure and flexural behavior of 3D printed PLA thermoplastic parts processed by fusion deposition modeling,” *AIMS Mater. Sci.*, vol. 6, no. 6, pp. 1033–1048, 2019,
- [27] K.-S. Seol, P. Zhao, B.-C. Shin, and S.-U. Zhang, “Infill Print Parameters for Mechanical Properties of 3D Printed PLA Parts,” *Korean Soc. Manuf. Process Eng.*, vol. 17, no. 4, pp. 9–16, Aug. 2018,

- [28] M. Heidari-Rarani, P. Sadeghi, and N. Ezati, “Effect of processing parameters on tensile properties of FDM 3D printed of PLA specimens,” *J. Sci. Technol. Compos.*, vol. 7, no. 2, pp. 855–862, 2020,
- [29] D. Farbman and C. McCoy, “Materials Testing of 3D Printed ABS and PLA Samples to Guide Mechanical Design,” Jun. 2016.
- [30] M. Kamaal, M. Anas, H. Rastogi, N. Bhardwaj, and A. Rahaman, “Effect of FDM process parameters on mechanical properties of 3D-printed carbon fibre–PLA composite,” *Prog. Addit. Manuf.*, vol. 6, no. 1, pp. 63–69, Feb. 2021,
- [31] A. H. K.A. Wahid , Z. Puteh , W.M. Wan Muhamad , A.R. Irfan , “COMPUTATIONAL MODELLING AND CHARACTERIZATION OF STRESS CONCENTRATION OF LINE PATTERN AT VARIOUS ANGLE ORIENTATION FOR CYCLIC LOADING,” *PalArch’s J. Archaeol. Egypt / Egyptol.*, vol. 17, no. 9 SE-, pp. 4068–4084, Nov. 2020.
- [32] J. T. Cantrell *et al.*, “Experimental characterization of the mechanical properties of 3D-printed ABS and polycarbonate parts,” *Rapid Prototyp. J.*, vol. 23, no. 4, pp. 811–824, Jun. 2017,
- [33] S. R. Rajpurohit and H. K. Dave, “Analysis of tensile strength of a fused filament fabricated PLA part using an open-source 3D printer,” *Int. J. Adv. Manuf. Technol.*, no. 101, pp. 1525–1536, 2019,
- [34] A. A. Ansari and M. Kamil, “Effect of print speed and extrusion temperature on properties of 3D printed PLA using fused deposition modeling process,” *Mater. Today Proc.*, vol. 45, pp. 5462–5468, 2021,
- [35] C. K. Yeoh, C. S. Cheah, R. Pushpanathan, C. C. Song, M. A. Tan, and P. L. Teh, “Effect of infill pattern on mechanical properties of 3D printed PLA and cPLA,” *IOP Conf. Ser. Mater. Sci. Eng.*, vol. 957, p. 012064, Nov. 2020,

- [36] J. M. Chacón, M. A. Caminero, E. García-Plaza, and P. J. Núñez, “Additive manufacturing of PLA structures using fused deposition modelling: Effect of process parameters on mechanical properties and their optimal selection,” *Mater. Des.*, vol. 124, pp. 143–157, Jun. 2017,
- [37] S. H. Masood, K. Mau, and W. Q. Song, “Tensile Properties of Processed FDM Polycarbonate Material,” *Mater. Sci. Forum*, vol. 654–656, pp. 2556–2559, Jun. 2010,
- [38] W. Wu, W. Ye, Z. Wu, P. Geng, Y. Wang, and J. Zhao, “Influence of Layer Thickness, Raster Angle, Deformation Temperature and Recovery Temperature on the Shape-Memory Effect of 3D-Printed Polylactic Acid Samples,” *Materials (Basel)*, vol. 10, no. 8, p. 970, Aug. 2017,
- [39] D. Syrlybayev, B. Zharylkassyn, A. Seisekulova, M. Akhmetov, A. Perveen, and D. Talamona, “Optimisation of Strength Properties of FDM Printed Parts—A Critical Review,” *Polymers (Basel)*, vol. 13, no. 10, p. 1587, May 2021,
- [40] Z. Shen, H. Hua, S. Yang, and Y. Zhang, “Effect of Fabrication Parameters and Material Features on Tensile Strength of FDM Built Parts,” *IOP Conf. Ser. Mater. Sci. Eng.*, vol. 423, p. 012050, Nov. 2018,
- [41] M. S. Chaudhry and A. Czekanski, “Evaluating FDM Process Parameter Sensitive Mechanical Performance of Elastomers at Various Strain Rates of Loading,” *Materials (Basel)*, vol. 13, no. 14, p. 3202, Jul. 2020,
- [42] C. Lubombo and M. Huneault, “Effect of infill patterns on the mechanical performance of lightweight 3D-printed cellular PLA parts,” *Mater. today Commun.*, vol. 17, pp. 214–228, 2018.
- [43] Y. Wang, P. Xue, and J. P. Wang, “Comparing Study of Energy-Absorbing Behavior for Honeycomb Structures,” *Key Eng. Mater.*, vol. 462–463, pp. 13–

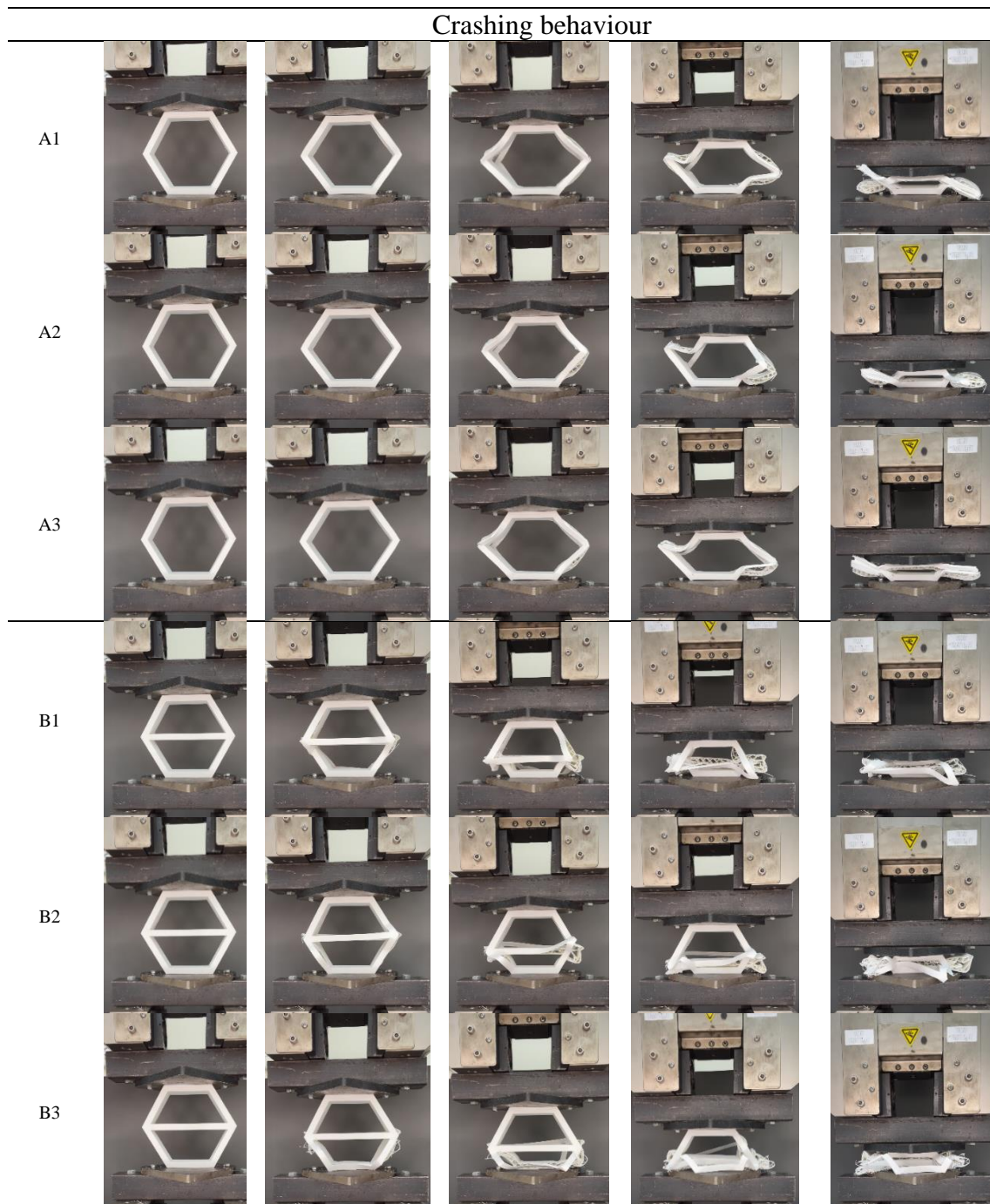
- 17, Jan. 2011,
- [44] F. N. Habib, P. Iovenitti, S. H. Masood, and M. Nikzad, “Cell geometry effect on in-plane energy absorption of periodic honeycomb structures,” *Int. J. Adv. Manuf. Technol.*, vol. 94, no. 5–8, pp. 2369–2380, Feb. 2018,
- [45] F. N. Habib, P. Iovenitti, S. H. Masood, and M. Nikzad, “In-plane energy absorption evaluation of 3D printed polymeric honeycombs,” *Virtual Phys. Prototyp.*, vol. 12, no. 2, pp. 117–131, Apr. 2017,
- [46] S. Antony, A. Cherouat, and G. Montay, “Fabrication and Characterization of Hemp Fibre Based 3D Printed Honeycomb Sandwich Structure by FDM Process,” *Appl. Compos. Mater.*, vol. 27, no. 6, pp. 935–953, Dec. 2020,
- [47] J. Podroužek, M. Marcon, K. Ninčević, and R. Wan-Wendner, “Bio-Inspired 3D Infill Patterns for Additive Manufacturing and Structural Applications,” *Materials (Basel)*, vol. 12, no. 3, 2019,
- [48] C. Yang, H. D. Vora, and Y. Chang, “Behavior of auxetic structures under compression and impact forces,” *Smart Mater. Struct.*, vol. 27, no. 2, p. 025012, Feb. 2018,
- [49] R. V. Duraibabu, R. Prithvirajan, M. Sugavaneswaran, and G. Arumaikkannu, “Compression behavior of Functionally Graded Cellular Materials fabricated with FDM,” *Mater. Today Proc.*, vol. 24, pp. 1035–1041, Jan. 2020,
- [50] J. J. Andrew, H. Alhashmi, A. Schiffer, S. Kumar, and V. S. Deshpande, “Energy absorption and self-sensing performance of 3D printed CF/PEEK cellular composites,” *Mater. Des.*, vol. 208, p. 109863, Oct. 2021,
- [51] S. Sawant, “What is Rhinoceros 3D? A 3D Modeling Software Based on NURBS Geometry,” 2021. <https://parametric-architecture.com/what-is-rhinoceros-3d-a-3d-modeling-software-based-on-nurbs-geometry/>

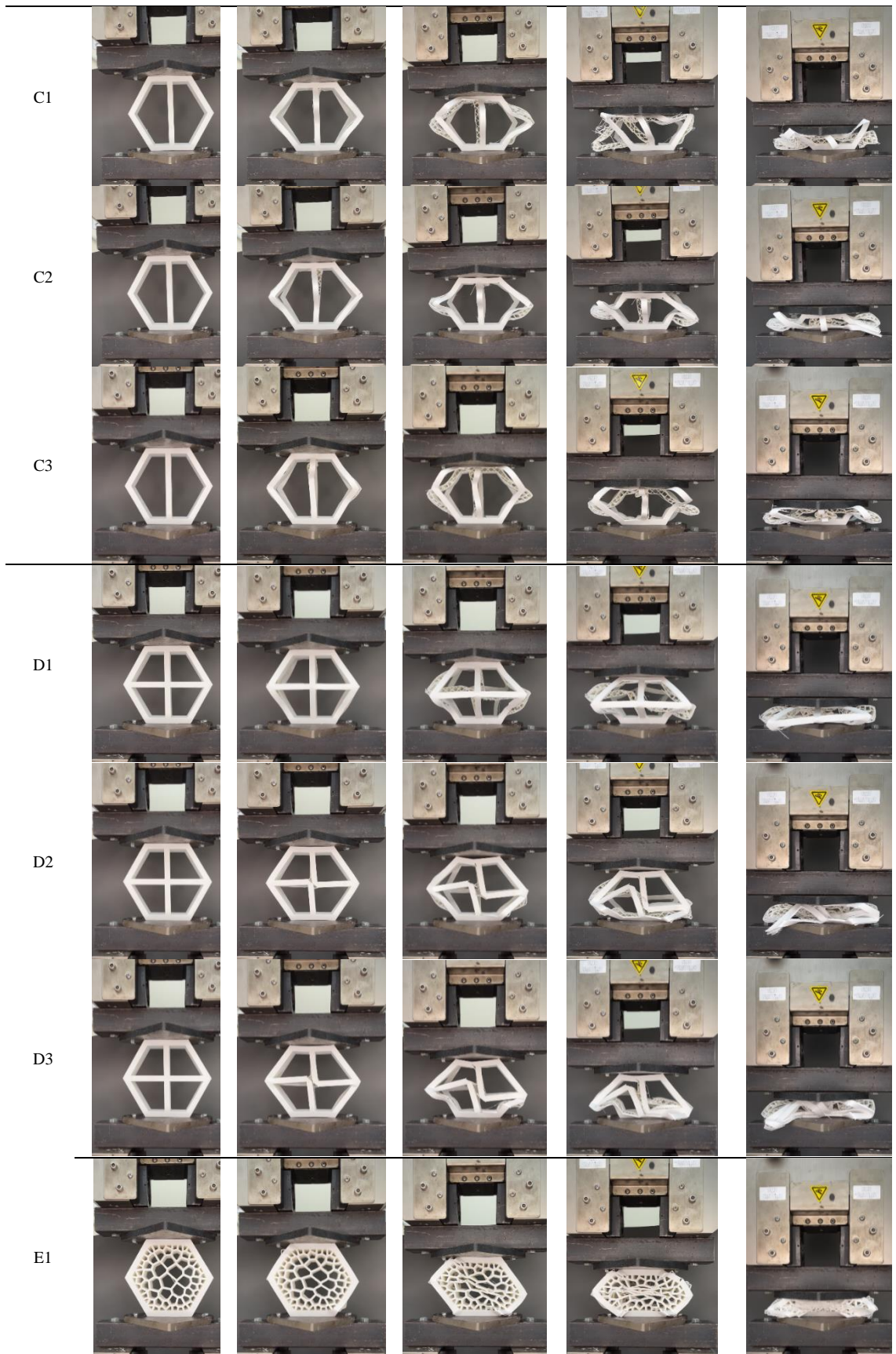
- [52] S. Sawant, “Grasshopper 3D: A Modeling Software Redefining The Design Process,” 2021. <https://parametric-architecture.com/grasshopper-3d-a-modeling-software-redefining-the-design-process/>
- [53] A. Lanzotti, M. Grasso, G. Staiano, and M. Martorelli, “The impact of process parameters on mechanical properties of parts fabricated in PLA with an open-source 3-D printer,” *Rapid Prototyp. J.*, vol. 21, no. 5, pp. 604–617, Aug. 2015,
- [54] S. Brischetto and R. Torre, “Tensile and Compressive Behavior in the Experimental Tests for PLA Specimens Produced via Fused Deposition Modelling Technique,” *Journal of Composites Science*, vol. 4, no. 3. 2020.
- [55] “ASTM D638 - 14 Standard Test Method for Tensile Properties of Plastics.” <https://www.astm.org/Standards/D638.htm> (accessed Oct. 03, 2021).
- [56] “ASTM D695 - 15 Standard Test Method for Compressive Properties of Rigid Plastics.” <https://www.astm.org/Standards/D695.htm> (accessed Oct. 04, 2021).
- [57] M. R. Nurul Fazita, H. P. S. Abdul Khalil, A. Nor Amira Izzati, and S. Rizal, “3 - Effects of strain rate on failure mechanisms and energy absorption in polymer composites,” in *Woodhead Publishing Series in Composites Science and Engineering*, M. Jawaid, M. Thariq, and N. B. T.-F. A. in B. Saba Fibre-Reinforced Composites and Hybrid Composites, Eds. Woodhead Publishing, 2019, pp. 51–78.

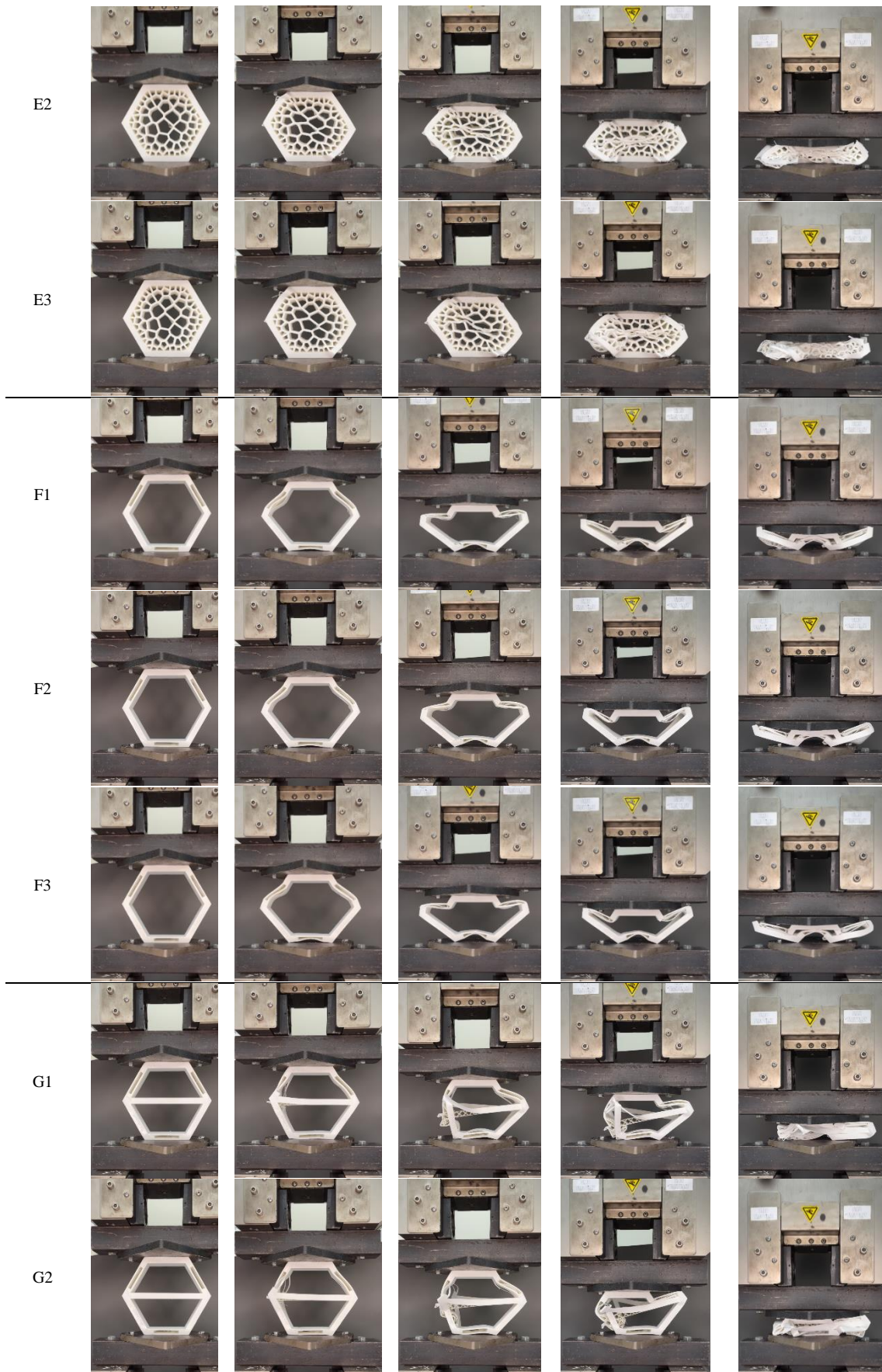
APPENDIX A: THE CRUSHING BEHAVIOUR UNDER COMPRESSION

In this appendix, the visual results of the in-plane compression test for each sample have been summarized in Table 11, as five snapshots for each specimen have been included in order to presents the crashing behaviour.

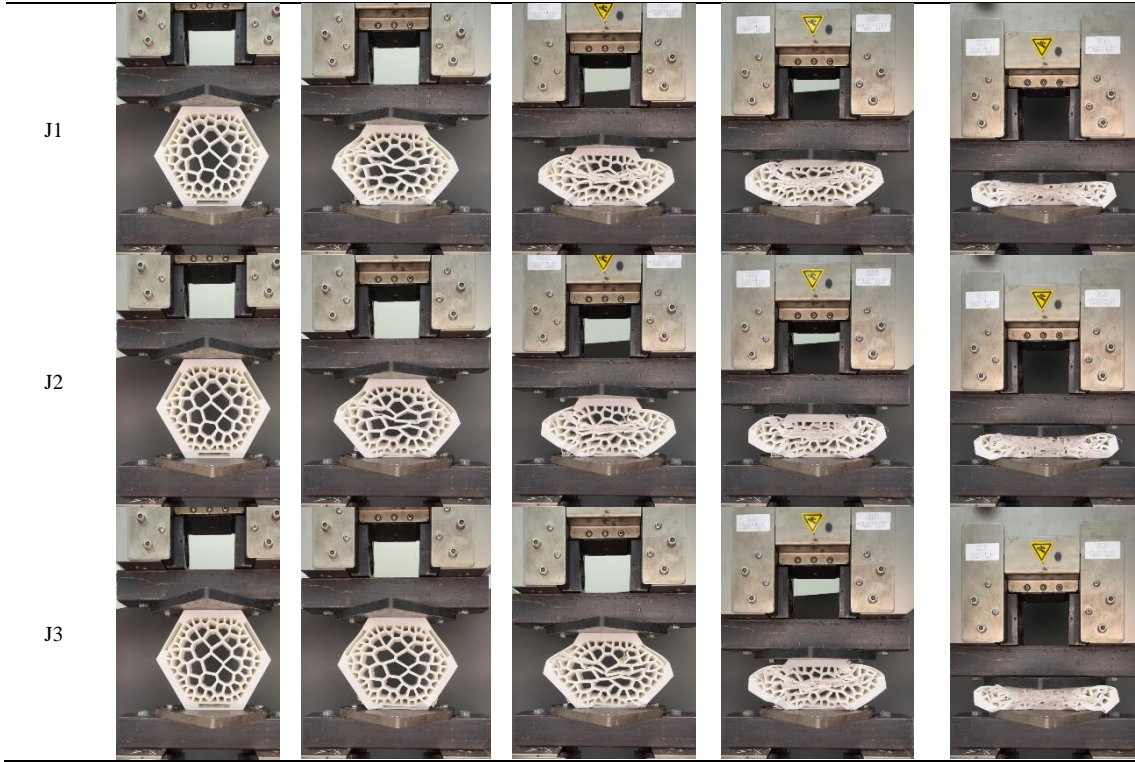
Table 11: Crushing behaviour of all honeycomb samples with different configurations under quasi-static axial compression.











APPENDIX B: AVERAGE FORCE AND DISPLACEMENT CURVES

In this appendix, the average of absorbed energy has been calculated for each configuration, then plotted with all other configurations, as seen in Figures Figure 47 and Figure 48.

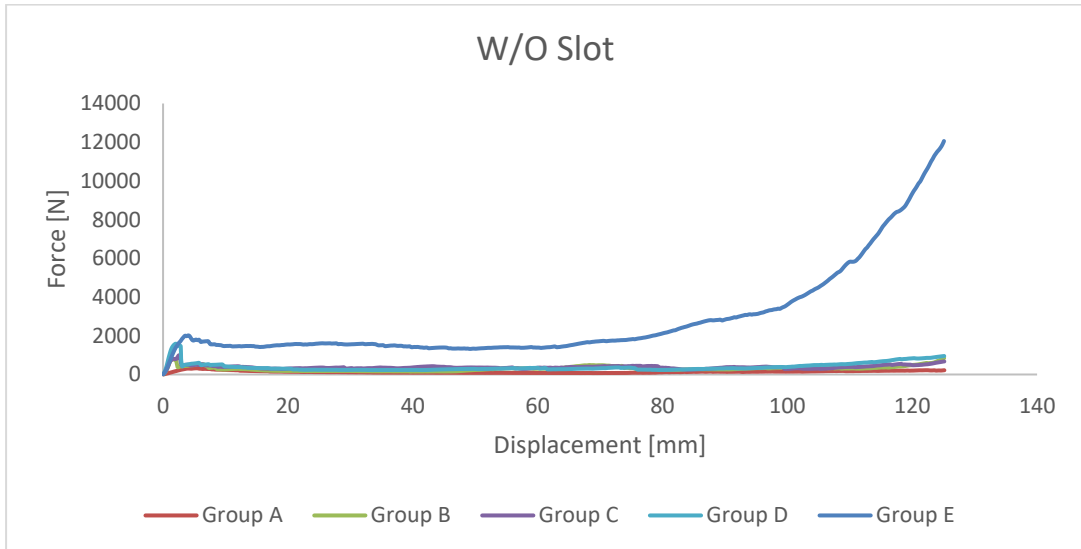


Figure 47: Average Force and displacement curves for all Groups, while slots are not included.

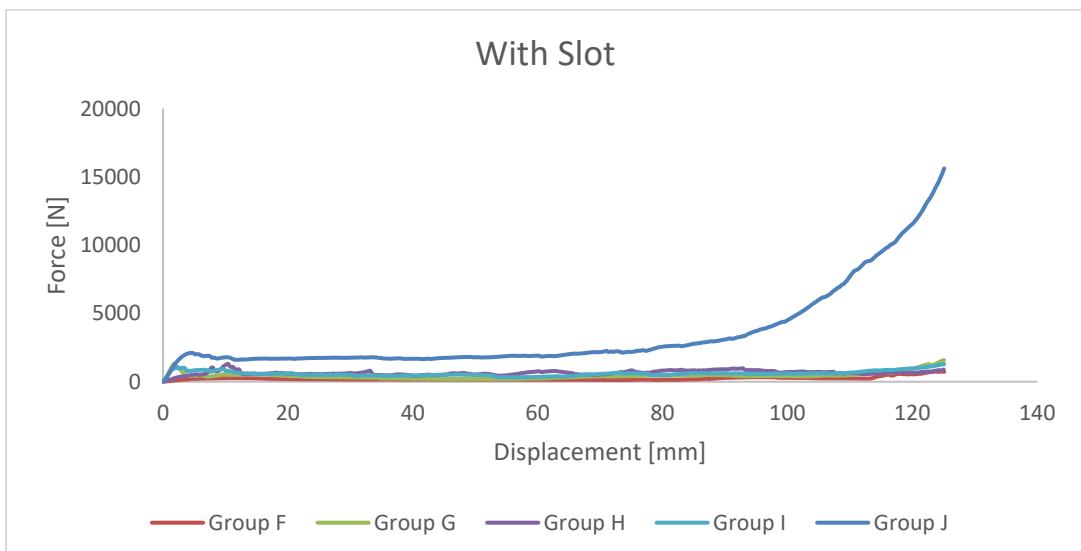


Figure 48: Average Force and displacement curves for all Groups, while slots are included.

APPENDIX C: SOME PRINTED SAMPLES THAT OBTAINED DURING THE
TRIAL-AND-ERROR PHASE

Here in this appendix, I am reporting some of the printed samples in different settings that the ones that has been mentioned in Table 2, as this phase was part of the trial-and-error phase. Figure 49 shows printed samples with different infill percentage and Figure 50 shows printed samples with different layer height as well.

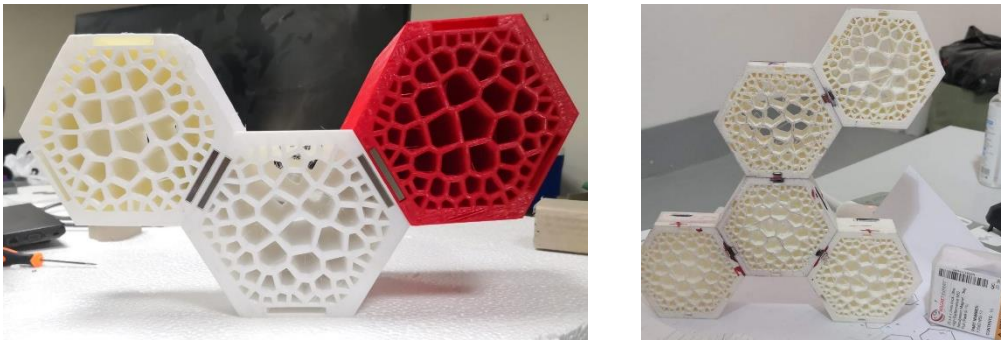


Figure 49: Printed samples with different infill.

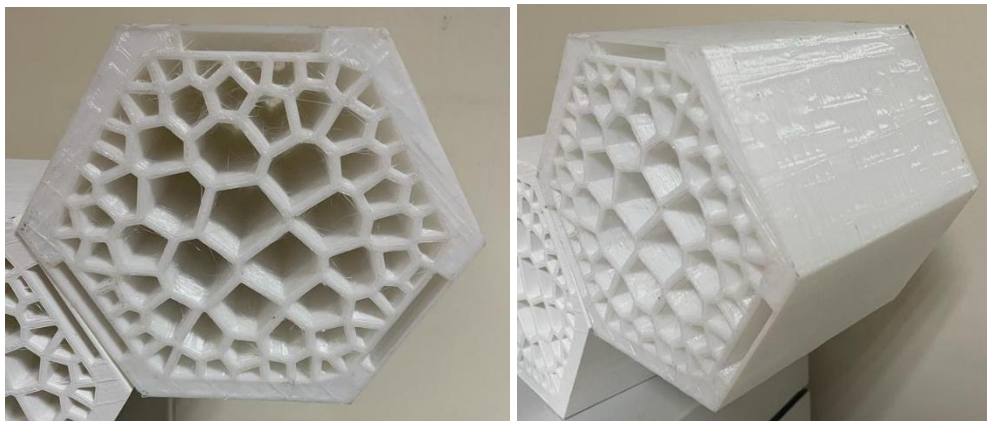


Figure 50: Printed samples with different layer heights